



<https://technobius.kz/>

e-ISSN
2789-7338

Technobius

A peer-reviewed open-access journal

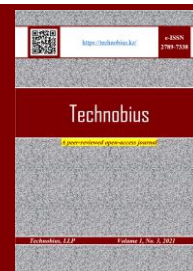
Technobius, LLP

Volume 5, No. 2, 2025



Technobius

Volume 5, No. 2, 2025



A peer-reviewed open-access journal registered by the Ministry of Culture and Information of the Republic of Kazakhstan, Certificate № KZ26VPY00087928 dated 21.02.2024




ISSN (Online): 2789-7338

Thematic Directions: Construction, Materials Science




Publisher: Technobius, LLP

Address: 2 Turkestan street, office 116, 010000, Astana, Republic of Kazakhstan




Editor-in-Chief:




   **Yelbek Utepov**, PhD, Professor, Department of Civil Engineering, L.N. Gumilyov Eurasian National University, Astana, Kazakhstan




Editors:




   **Assel Tulebekova**, PhD, Professor, Department of Civil Engineering, L.N. Gumilyov Eurasian National University, Astana, Kazakhstan




   **Victor Kaliakin**, PhD, Professor, Department of Civil, Construction, and Environmental Engineering, University of Delaware, Newark, DE, USA




   **Askar Zhussupbekov**, Doctor of Technical Sciences, Professor, Department of Civil Engineering, L.N. Gumilyov Eurasian National University, Astana, Kazakhstan




   **Talal Awwad**, Doctor of Technical Sciences, Professor, Department of Geotechnical Engineering, Damascus University, Damascus, Syria




   **Ignacio Menéndez Pidal de Navascués**, Doctor of Technical Sciences, Professor, Department of Civil Engineering, Technical University of Madrid, Madrid, Spain




   **Daniyar Akhmetov**, Doctor of Technical Sciences, Associate Professor, Department of Construction and Building materials, Satbayev University, Almaty, Kazakhstan

   **Zhanbolat Shakhmov**, PhD, Associate Professor, Department of Civil Engineering, L.N. Gumilyov Eurasian National University, Astana, Kazakhstan

   **Timoth Mkilima**, PhD, Lecturer, Department of Environmental Engineering and Management, the University of Dodoma, Dodoma, Tanzania

   **Aliya Aldungarova**, PhD, Associate Professor, Department of Mining, Construction and Ecology of S. Sadvakasov Agrotechnical Institute of Kokshetau University named after Sh. Ualikhanov, Kokshetau, Kazakhstan

   **Raikhan Tokpatayeva**, PhD, Senior Lab Operations Specialist (affiliated with Pankow Materials Lab), Lyles School of Civil and Construction Engineering, Purdue University, West Lafayette, IN, USA

   **Ankit Garg**, Doctor of Engineering, Professor, Department of Civil and Environmental Engineering, Shantou University, Shantou, China

Copyright: © Technobius, LLP

Contacts: Website: <https://technobius.kz/>
E-mail: technobius.research@gmail.com

CONTENTS

Title and Authors	Category	No.
Spatial interpolation of the latest Quaternary and older Mesozoic sediment soils <i>Akmaral Yeleussinova, Nurgul Shakirova, Nurgul Alibekova, Sabit Karaulov</i>	<i>Construction</i>	0077
Improvement of the crack resistance of reinforced concrete sleepers using modified concretes <i>Ilyas Abdraimov, Kuttybay Musa, Ibrahim Kasimov, Mariya Sailygarayeva, Vladislav Pak, Yerkyn Turarov</i>	<i>Construction</i>	0078
Studying the material orthotropy effect under the plane stress state of triangular plates <i>Moldir Beketova, Zhmagul Nuguzhinov, Serik Akhmediyev, Valentin Mikhailov, Omirkhan Khabidolda</i>	<i>Construction, Materials Science</i>	0079
Effect of paraffine wax on the mobility of injection cement mortars <i>Zhibek Zhantlessova, Rauan Lukpanov, Duman Dyusseminov, Serik Yenkebayev, Denis Tsygulyov, Murat Karacasu</i>	<i>Materials Science</i>	0080
Investigation of the properties of fly ash and slag-based geopolymer concrete containing waste glass aggregates <i>Zhuzimkul Urkinbayeva, Assel Jexembayeva, Marat Konkanov, Samal Akimbekova, Lailya Zhaksylykova, Tariq Umar</i>	<i>Materials Science</i>	0081
Corrigendum to “A. Omarov and Y. Iwasaki, “Comparative study of pile quality control techniques”, <i>tbus</i> , vol. 4, no. 1, p. 0055, Mar. 2024. doi: 10.54355/tbus/4.1.2024.0055” <i>Abdulla Omarov, Yoshinori Iwasaki</i>	<i>Construction</i>	0082



Spatial interpolation of the latest Quaternary and older Mesozoic sediment soils

Akmaral Yeleussinova¹, Nurgul Shakirova^{1,*}, Nurgul Alibekova¹, Sabit Karaulov²

¹Department of Civil Engineering, L.N. Gumilyov Eurasian National University, Astana, Kazakhstan

²Solid Research Group, LLP, Astana, Kazakhstan

*Correspondence: nur_shakirova77@mail.ru

Abstract. The paper presents a comparison of three methods of interpolation of engineering-geological parameters of soils: Empirical Bayesian Kriging (EBK), ordinary Kriging, and Inverse Distance Weighting (IDW). The initial data were obtained from bored wells on the territory of the residential complex in Astana city. Interpolation was performed along a horizontal section at a depth of 10 m for the parameters: cohesion, modulus of deformation, and friction angle. The results were visualized as heatmaps. Comparative analysis showed that the EBK 3D method provides a higher degree of detail and robustness to insufficient data density compared to IDW and Kriging, making it the most preferred method for 3D modeling of soil mechanical properties.

Keywords: soils, mechanical properties, spatial interpolation, GIS, lithology.

1. Introduction

The current state of engineering-geological surveys is increasingly determined by the need to integrate classical methods of field and laboratory studies with digital technologies of spatial analysis [1], [2]. Increase in urban density, intensification of urban planning processes, implementation of large-scale infrastructure projects, especially in conditions of cramped city development and complex engineering and geological conditions, impose new requirements for accuracy, detail, and reproducibility of subsurface space modeling [3], [4], [5], [6].

One of the most promising approaches to solving these problems is three-dimensional modeling of the geological environment [7]. Unlike traditional stratigraphic, block, or surface models, 3D structures form a regular grid covering the study area with a given spatial resolution [8]. This is especially important when modeling natural environments characterized by pronounced heterogeneity and anisotropy [9], [10]. A key step in building a 3D model is interpolation, a procedure for estimating parameter values at points not covered by direct measurements [9]. This task presents significant challenges given the limited and irregular spatial distribution of field observations (e.g., boreholes) and because of the stochastic nature of engineering geologic properties in the natural environment [11]. Under such conditions, the choice of interpolation method becomes crucial: it determines the accuracy and reliability of the generated model and, consequently, the validity of design and engineering decisions made on its basis [12].

Despite the widespread use and development of the mathematical apparatus of these methods, the comparative effectiveness of their application to real geotechnical data remains an open question in geotechnical engineering practice [13], [14]. This is especially true under conditions where observations are limited and the spatial structure of the massif under study is complex and poorly defined [15]. The available literature presents mostly theoretical justifications of interpolation algorithms, such as Inverse Distance Weighting (IDW), ordinary Kriging, and Empirical Bayesian Kriging 3D (EBK); or individual practical examples of their application without a comprehensive

analysis of accuracy, robustness to outliers, sensitivity to density, and configuration of observation points [16], [17]. In geotechnical engineering applications, where each estimate may have critical implications for strength, stability, or settlement calculations, such analysis takes on applied significance [18], [19], [20].

This study aims to conduct a comparative analysis of interpolation methods: IDW, Kriging, EBK, from the perspective of their applicability for estimation of intermediate values of geotechnical properties in a complex and heterogeneous geological structure.

2. Methods

2.1 Initial data

The materials of engineering-geological surveys and the results of the topographic survey of the territory intended for the construction of a multifunctional residential complex located in Astana, Saryarka district, Republic of Kazakhstan, were used as input data. In the course of survey works, 5 engineering-geological boreholes were drilled, the results of which established the occurrence of five engineering-geological elements (EGE) formed in the conditions of the latest Quaternary and older Mesozoic sediments. The lithology composition and engineering-geological characteristics of each element are described below (Figure 1).

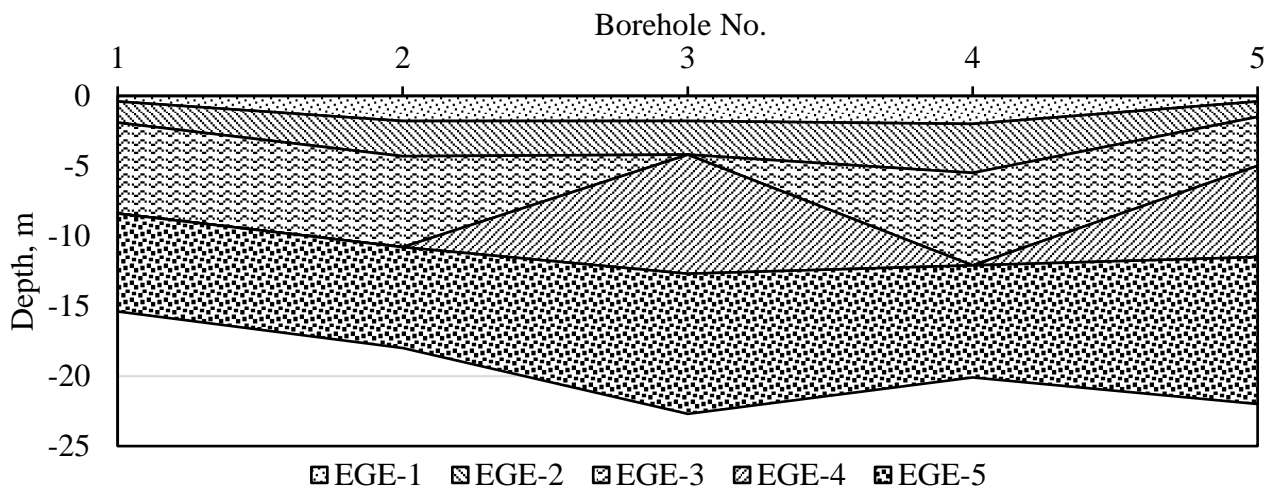


Figure 1 – Lithology section of surveyed site

EGE-1 (laQIII-IV) is represented by water-saturated loams of light brown color. The consistency varies from hard to soft plastic. It contains organic inclusions up to 4.10%. There are interlayers of sand and sandy loam. It was formed under conditions of alluvial-deluvial sedimentation. EGE-2 (laQIII-IV) is composed of light-brown and brown-colored water-saturated sandy loam. The consistency varies from solid to fluid. The content of organic matter reaches 3.20%. There are interlayers of sand and loam. The sediments are of alluvial origin. EGE-3 (laQIII-IV) is represented by sands of medium coarseness, light brown and brown, saturated with water. Interlayers of sand of different coarseness are noted in the composition. It was formed under alluvial conditions with a variable hydrodynamic regime. EGE-4 (laQIII-IV) is composed of gravelly sands of light-brown and brown color, water-saturated. It has inclusions and interlayers of sands of different coarseness. Deposits characteristic of channel and near-channel alluvial facies. EGE-5 (eMZ) is represented by clays of light brown and light yellowish-brown color, in some places with a dark gray tint. The clays are water-saturated, of hard consistency, with areas of iron and manganese, inclusions of tar sands, and interlayers of loam. Lower Mesozoic sediments are characterized by significant density and low filtration capacity.

The data presented in tabular form were used for spatial analysis. Thus, Table 1 contains engineering-geological data obtained from the results of borehole drilling. For each borehole, the

coordinates (latitude and longitude in the WGS 84 coordinate system), as well as the main mechanical characteristics of the soils in the selected EGEs, were indicated.

Table 1 – Borehole soil characterization data template

Borehole No.	Latitude	Longitude	Soil type 1				Soil type 2				Soil type m			
			φ_1	E_1	c_1	h_1	φ_2	E_2	c_2	h_2	φ_n	E_n	c_n	h_n
1	71.42976435	51.06208017	0	1.3	20	5	6	14	14	3	0	0	0	6
2	71.43025677	51.06210828	0	0	0	10	3.3	20	12.7	9	0	0	0	8
3	71.4307321	51.0619152	0	5	12	15	0	0	0	12	0	0	30	13
...
n	71.43086928	51.06203564	0	5	12	20	8	15	17	18	21	30	30	19

Interpolation was done in ArcGIS Pro using the Spatial Analyst and Geostatistical Analyst tools using three methods.

2.2 IDW interpolation

The IDW principle is that the values of the interpolated parameter at an unknown point are defined as a weighted average of the values at known points, with the weight inversely proportional to the distance to the power of p (Eq. (1)) [21].

$$z(x_0) = \frac{\sum_{i=1}^n \gamma_i z(x_i)}{\sum_{i=1}^n \gamma_i}, \gamma_i = \frac{1}{d(x_0, x_i)^p}, \quad (1)$$

where: $z(x_0)$ – value at interpolated point; γ_i – weight; $z(x_i)$ – value at existing point i ; $d(x_0, x_i)^p$ – distance between points; p – degree of influence (commonly is 2); n number of nearest points.

2.3 Ordinary Kriging interpolation

Ordinary Kriging is based on constructing a spatial autocorrelation model using variograms and minimizing the variance of the estimation error (Eq. (2)) [22].

$$z(x_0) = \sum_{i=1}^n \lambda_i z(x_i), \sum_{i=1}^n \lambda_i = 1, \quad (2)$$

where the coefficient λ_i determined by solving the system of linear equations based on the variogram model (Eq. (3)).

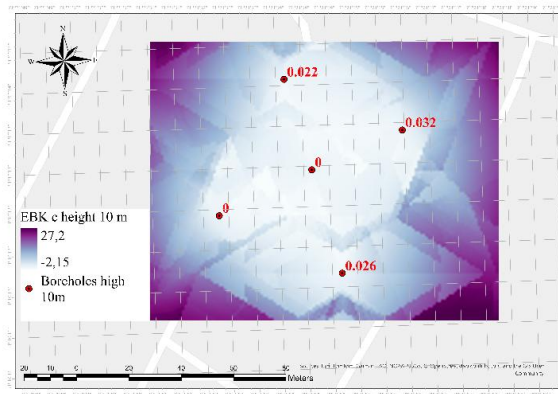
$$\gamma(h) = \frac{1}{2} E \left[(Z(x) - Z(x+h))^2 \right] \quad (3)$$

2.4 EBK 3D interpolation

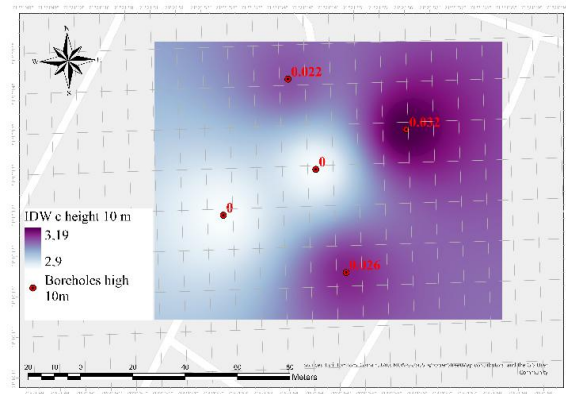
EBK uses a Bayesian approach to variogram generation, where model parameters are estimated not once, but over multiple subsamples with subsequent averaging: automatic variogram generation; accounting for model uncertainty; more robust to localized outliers and unstable data structure. A special feature of the EBK method is the automatic accounting of boundary conditions and model uncertainty through the use of Extents, which allows for a more accurate description of parameter distributions in areas with sparse data. The spatial location of wells is fixed in the WGS 84 (or UTM Zone) coordinate system of the corresponding region [23].

3. Results and Discussion

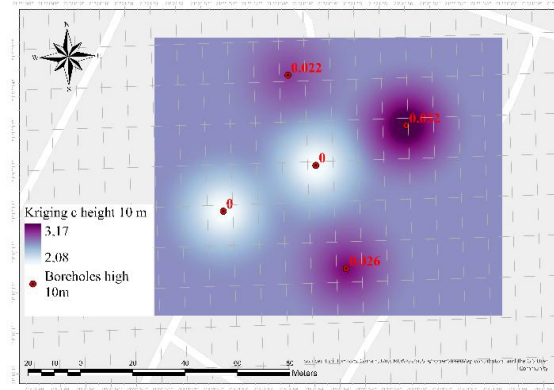
As a result of processing of field data obtained during engineering geological surveys, heatmaps of the spatial distribution of key mechanical characteristics of soils at a depth of 10 m were constructed through interpolations of EBK, Kriging, and IDW. Thus, Figures 2a, 2b, and 2c show the distributions of specific cohesion (c), where the range of values varies from -2.15 to 27.2 kPa. Figures 3a, 3b, and 3c show the distribution of strain modulus (E), where the values range from 0 to 33 MPa. Figures 4a, 4b, and 4c show the interpolation of the angle of internal friction (φ), whose values range from 0 to 25 degrees.



a) EBK

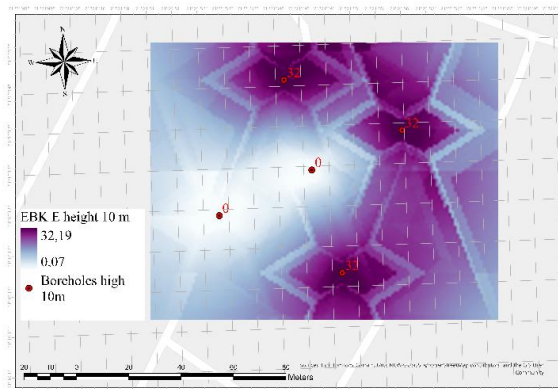


b) IDW

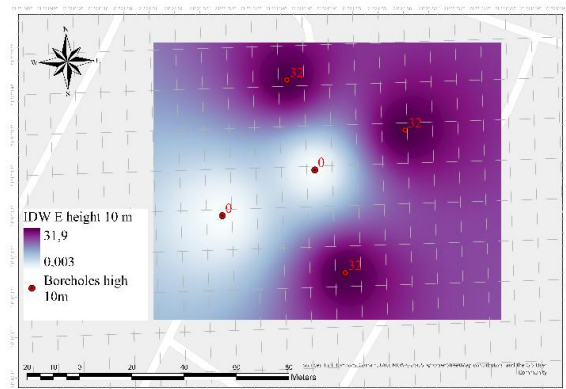


c) Ordinary Kriging

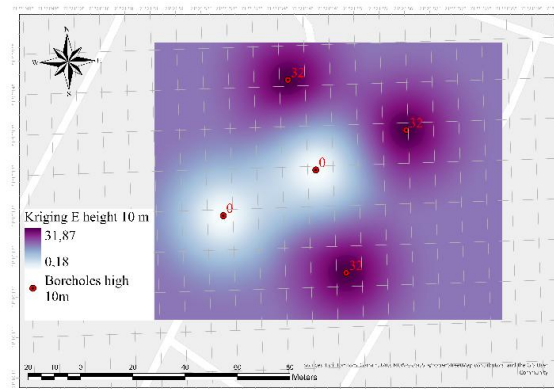
Figure 2 – Distribution of c at 10 m depth



a) EBK

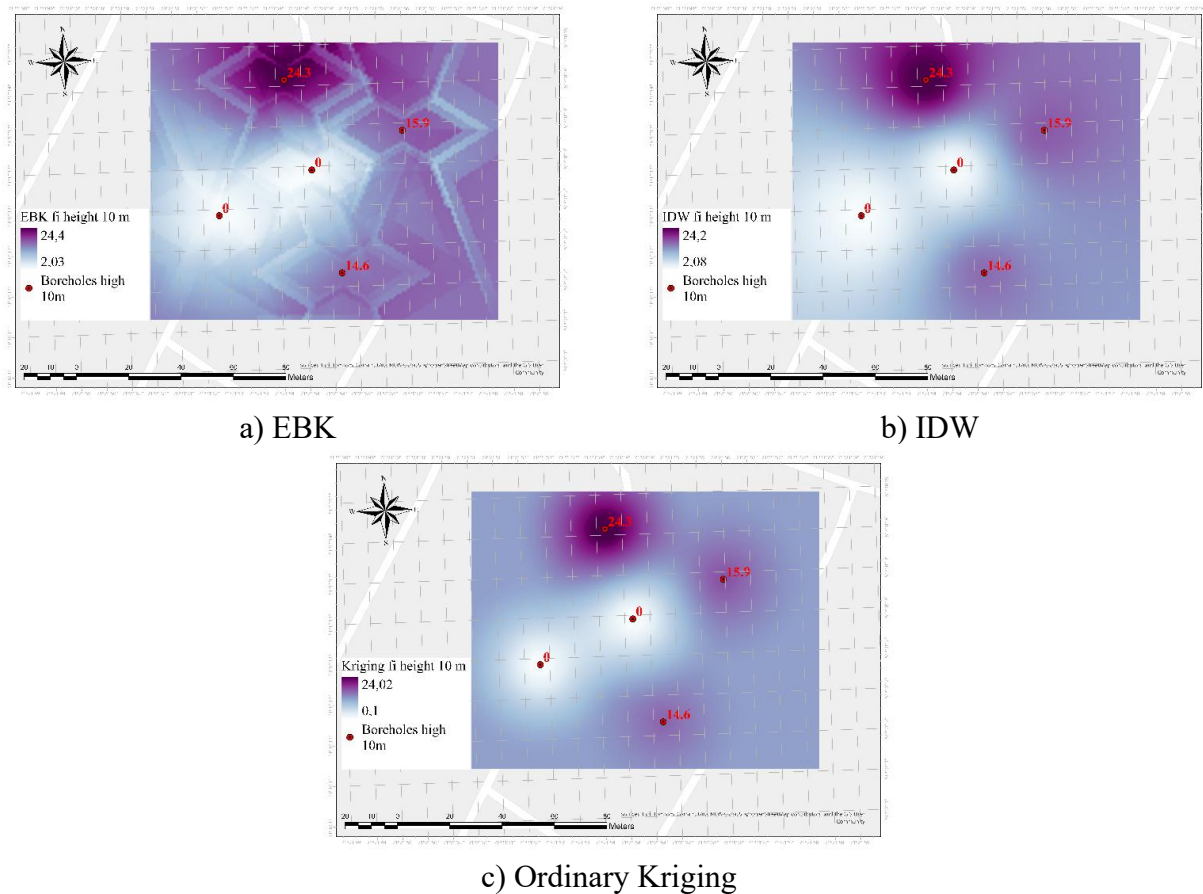


b) IDW



c) Ordinary Kriging

Figure 3 – Distribution of E at 10 m depth

Figure 4 – Distribution of ϕ at 10 m depth

Visual examination of the interpolated data obtained in the form of heatmaps revealed several qualitative differences between the models. The IDW model was characterized by pronounced zonality and local variability. The most noticeable were artifacts in the form of "spots" in zones with low density of points (wells), which reflects the excessive influence of the nearest measurements and lack of consideration of spatial correlation. The model based on ordinary Kriging showed a smoother distribution of values over the volume. However, over-simplification was observed in areas devoid of observational data: the method tended to average values, losing the ability to detect local anomalies. In addition, the quality of the result depended significantly on the accuracy of manual variogram adjustment, which increases the subjectivity of the model. The best structural consistency was achieved using the EBK method. The Bayesian stochastic approach underlying the algorithm allowed not only to automate the stage of variogram construction, but also to take into account spatial heterogeneity in poorly studied areas. Visually, the model was characterized by a high degree of detail, especially in the zones of abrupt parameter changes, and at the same time by the absence of over-averaging. The obtained results are consistent with those of previous studies [17], [19] and supplement strengthen them with additional case at the Quaternary and Mesozoic soils.

4. Conclusions

The study demonstrated the possibility of defining the mechanical properties of soils at unknown positions in the subsurface between the known ones (i.e., intermediate) with a certain quality extent using various methods, including the Inverse Distance Weighting, ordinary Kriging, and Empirical Bayesian Kriging.

Analysis of the interpolated models revealed fundamental differences in the behavior of each method. The IDW method showed the greatest sensitivity to local values and point density, which

was reflected in pronounced fragmentation and artifacts in the form of spots in areas poorly represented by wells. The Kriging method provided a more uniform distribution of parameters, but demonstrated a tendency to average values, especially in zones with low data density, which reduces its ability to detect local anomalies. The most balanced and structurally consistent results were obtained using the EBK method, which achieved a high degree of detail without excessive fragmentation or smoothing.

EBK 3D method can be recommended as the most reliable tool for spatial modeling of engineering-geological characteristics of soils, especially in conditions of a sparse well network and pronounced geological heterogeneity.

Acknowledgments

This research was funded by the Science Committee of the Ministry of Science and Higher Education of the Republic of Kazakhstan (Grant No. AP19676116).

References

- [1] R. R. Jones, K. J. W. McCaffrey, R. W. Wilson, and R. E. Holdsworth, "Digital field data acquisition: towards increased quantification of uncertainty during geological mapping," *Geological Society, London, Special Publications*, vol. 239, no. 1, pp. 43–56, Jan. 2004, doi: 10.1144/GSL.SP.2004.239.01.04.
- [2] Y. Utepov *et al.*, "Prototyping an integrated IoT-based real-time sewer monitoring system using low-power sensors," *Eastern-European Journal of Enterprise Technologies*, vol. 3, no. 5 (123), pp. 6–23, Jun. 2023, doi: 10.15587/1729-4061.2023.283393.
- [3] M. Al-Arafat, M. E. Kabir, A. Morshed, and M. A. U. Sunny, "Geotechnical Challenges In Urban Expansion: Addressing Soft Soil, Groundwater, And Subsurface Infrastructure Risks In Mega Cities," *Innovatech Engineering Journal*, vol. 1, no. 01, pp. 205–222, Nov. 2024, doi: 10.70937/itej.v1i01.20.
- [4] Zh. S. Nuguzhinov, A. T. Mukhamejanova, D. T. Tokanov, Z. Koishybay, N. Z. Zhumadilova, and M. S. Beketova, "Comprehensive study of the bases and foundations of furnaces No. 61, 63 of the melting shop No. 6 of the Aksu Ferroalloy Plant in connection with the renovation," in *Smart Geotechnics for Smart Societies*, London: CRC Press, 2023, pp. 1309–1313. doi: 10.1201/9781003299127-190.
- [5] A. Z. Zhussupbekov, A. T. Mukhamejanova, and K. A. Abdrakhmanova, "Comprehensive study of the mutual influence of closely erected foundations of reconstructed buildings," in *Smart Geotechnics for Smart Societies*, London: CRC Press, 2023, pp. 519–522. doi: 10.1201/9781003299127-63.
- [6] A. Mukhamejanova, K. Abdrakhmanova, S. Toleubayeva, and A. Kozhas, "Foundation for waterlogged bases with conical void design," *Technobius*, vol. 3, no. 1, p. 0031, Feb. 2023, doi: 10.54355/tbus/3.1.2023.0031.
- [7] F. Jørgensen, R. R. Møller, L. Nebel, N.-P. Jensen, A. V. Christiansen, and P. B. E. Sandersen, "A method for cognitive 3D geological voxel modelling of AEM data," *Bulletin of Engineering Geology and the Environment*, vol. 72, no. 3–4, pp. 421–432, Dec. 2013, doi: 10.1007/s10064-013-0487-2.
- [8] Q. Chen, G. Liu, X. Li, Z. Zhang, and Y. Li, "A corner-point-grid-based voxelization method for the complex geological structure model with folds," *J Vis (Tokyo)*, vol. 20, no. 4, pp. 875–888, Nov. 2017, doi: 10.1007/s12650-017-0433-7.
- [9] J. Li, P. Liu, X. Wang, H. Cui, and Y. Ma, "3D geological implicit modeling method of regular voxel splitting based on layered interpolation data," *Sci Rep*, vol. 12, no. 1, p. 13840, Aug. 2022, doi: 10.1038/s41598-022-17231-x.
- [10] C. B. JONES, "Data structures for three-dimensional spatial information systems in geology," *International journal of geographical information systems*, vol. 3, no. 1, pp. 15–31, Jan. 1989, doi: 10.1080/02693798908941493.
- [11] H. H. Einstein and G. B. Baecher, "Probabilistic and statistical methods in engineering geology," *Rock Mech Rock Eng*, vol. 16, no. 1, pp. 39–72, Feb. 1983, doi: 10.1007/BF01030217.
- [12] M. Lepot, J.-B. Aubin, and F. Clemens, "Interpolation in Time Series: An Introductory Overview of Existing Methods, Their Performance Criteria and Uncertainty Assessment," *Water (Basel)*, vol. 9, no. 10, p. 796, Oct. 2017, doi: 10.3390/w9100796.
- [13] A. Baghbani, T. Choudhury, S. Costa, and J. Reiner, "Application of artificial intelligence in geotechnical engineering: A state-of-the-art review," *Earth Sci Rev*, vol. 228, p. 103991, May 2022, doi: 10.1016/j.earscirev.2022.103991.
- [14] E. S. Utenov, A. T. Mukhamedzhanova, and S. K. Abildin, "Concerning the use of soil deformation modulus in geotechnical design," in *Geotechnics Fundamentals and Applications in Construction: New Materials, Structures, Technologies and Calculations*, CRC Press, 2019, pp. 451–456. doi: 10.1201/9780429058882-86.
- [15] M. Dong, C. Neukum, H. Hu, and R. Azzam, "Real 3D geotechnical modeling in engineering geology: a case study from the inner city of Aachen, Germany," *Bulletin of Engineering Geology and the Environment*, vol. 74, no. 2, pp. 281–300, May 2015, doi: 10.1007/s10064-014-0640-6.

- [16] J. Li and A. D. Heap, "Spatial interpolation methods applied in the environmental sciences: A review," *Environmental Modelling & Software*, vol. 53, pp. 173–189, Mar. 2014, doi: 10.1016/j.envsoft.2013.12.008.
- [17] A. Mukhamejanova *et al.*, "Toward the use of an intermediate value of the modulus of deformation of soils in geotechnical design," *E3S Web of Conferences*, vol. 559, p. 01008, Aug. 2024, doi: 10.1051/e3sconf/202455901008.
- [18] J. Shang, L. J. West, S. R. Hencher, and Z. Zhao, "Geological discontinuity persistence: Implications and quantification," *Eng Geol*, vol. 241, pp. 41–54, Jul. 2018, doi: 10.1016/j.enggeo.2018.05.010.
- [19] A. Aldungarova, T. Muzdybayeva, A. Mukhamejanova, N. Alibekova, K. Moskalova, and S. Karaulov, "Examining intermediate soil properties variability through spatial interpolation methods in GIS," *Technobius*, vol. 4, no. 3, p. 0062, Sep. 2024, doi: 10.54355/tbus/4.3.2024.0062.
- [20] A. Aldungarova, A. Mukhamejanova, N. Alibekova, and A. Aniskin, "Ways to address the construction of new buildings in old urban areas," *Technobius*, vol. 3, no. 4, p. 0048, Dec. 2023, doi: 10.54355/tbus/3.4.2023.0048.
- [21] GISGeography, "Inverse Distance Weighting (IDW) Interpolation," GIS Analysis. Accessed: Aug. 25, 2019. [Online]. Available: <https://gisgeography.com/inverse-distance-weighting-idw-interpolation/>
- [22] A. Anand, P. Singh, P. K. Srivastava, and M. Gupta, "GIS-based analysis for soil moisture estimation via kriging with external drift," in *Agricultural Water Management*, Elsevier, 2021, pp. 391–408. doi: 10.1016/B978-0-12-812362-1.00019-9.
- [23] K. Krivoruchko, "Empirical Bayesian Kriging: Implemented in ArcGIS Geostatistical Analyst," *ArcUser*, vol. 15, no. 4, pp. 6–10, 2012.

Information about authors:

Akmaral Yeleussinova – Candidate of Technical Sciences, Head of the Department, Department of Civil Engineering, L.N. Gumilyov Eurasian National University, Astana, Kazakhstan, yeleussinova_aye@enu.kz

Nurgul Shakirova – PhD, Senior Lecturer, Department of Civil Engineering, L.N. Gumilyov Eurasian National University, Astana, Kazakhstan, nur_shakirova77@mail.ru

Nurgul Alibekova – PhD, Associate Professor, Department of Civil Engineering, L.N. Gumilyov Eurasian National University, Astana, Kazakhstan, nt_alibekova@mail.ru

Sabit Karaulov – Junior Researcher, Solid Research Group, LLP, Astana, Kazakhstan, karaulovsabit1997@gmail.com

Author Contributions:

Akmaral Yeleussinova – drafting, resources, editing, funding acquisition.

Nurgul Shakirova – concept, analysis, interpretation.

Nurgul Alibekova – testing, data collection.

Sabit Karaulov – methodology, drafting, visualization.

Conflict of Interest: The authors declare no conflict of interest.

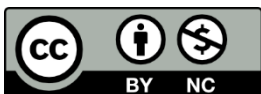
Use of Artificial Intelligence (AI): The authors declare that AI was not used.

Received: 16.01.2025

Revised: 03.05.2025

Accepted: 05.05.2025

Published: 05.05.2025



Copyright: © 2025 by the authors. Licensee Technobius, LLP, Astana, Republic of Kazakhstan. This article is an open access article distributed under the terms and conditions of the Creative Commons Attribution (CC BY-NC 4.0) license (<https://creativecommons.org/licenses/by-nc/4.0/>).



Improvement of the crack resistance of reinforced concrete sleepers using modified concretes

Ilyas Abdraimov¹, Musa Kuttybay¹, Ibrakhim Kasimov², Mariya Sailygarayeva^{3,*},
 Vladislav Pak⁴, Yerkyn Turarov⁴

¹Mukhtar Auezov South Kazakhstan Research University, Shymkent, Kazakhstan

²Tashkent University of Architecture and Civil Engineering, Tashkent, Uzbekistan

³The Kazakh National Agrarian Research University, Almaty, Kazakhstan

⁴International University of Transportation and Humanities, Almaty, Kazakhstan

*Correspondence: mariya_23365@mail.ru

Abstract. This paper presents research on the potential use of modified fiber-reinforced concrete for reinforced concrete sleepers, intending to increase their strength characteristics, crack resistance, and service life. To investigate the influence of reinforcing elements on the crack resistance of heavy concrete, chopped basalt fiber and, for comparison, polypropylene fiber were added to the concrete mix, both of which have shown promising performance. The results of the study showed that the modified heavy concrete exhibited improved crack resistance due to the formation of additional low-basic calcium hydrosilicates, compaction, and strengthening of the cement matrix, as well as the contribution of fibers to the formation of a spatially reinforced cement stone structure. The nature of the fracture of prism samples made from modified concrete and their crack resistance characteristics were evaluated. The results showed that samples with basalt fiber had a 40.59% increase in maximum load, a 40.5% increase in the conditional stress intensity factor, and a 40.49% increase in bending stress compared to the reference samples without fiber. In addition, the samples with basalt fiber demonstrated increases of 7.1%, 6.93%, and 6.9% in maximum load, bending stress, and stress intensity factor, respectively, compared to samples containing polypropylene fiber.

Keywords: modified fiber-reinforced concrete, reinforced concrete, crack resistance, concrete sleepers, fiber.

1. Introduction

It is known that railway sleepers, foundations of machines with dynamic loads, aerodrome and road slabs, and bridge structures are subjected to dynamic effects. Moreover, the sources of dynamic effects can be both external to the structures and internal, located inside the structure [1]. In turn, these loads can have different directions and the nature of application of loads to the structure – distributed load, moments, concentrated forces. As a result of the impact of these loads, there is an accumulation of damage at the micro-level, further development of which leads to the formation and opening of cracks, which significantly reduces the service life, load-bearing capacity, and the degree of resistance in aggressive environments. Reinforced concrete sleepers for railway lines are subject to a set of requirements for strength and crack resistance [2]. To improve the performance characteristics of concrete, fly ash, metakaolin, blast furnace slag, rice husk ash, amorphous microsilica, and other types of pozzolanic additives are introduced into the concrete mixture.

The solution to the problem of obtaining effective concrete for reinforced concrete railway sleepers with improved performance indicators in terms of strength and crack resistance can be achieved by densification and strengthening of the cement matrix structure through the joint application of condensed microsilica suspension with plasticizer and basalt fiber [3].

During the study of loads acting on heavy concrete products, in particular, reinforced concrete sleepers working in special operating conditions, resistance to dynamic effects is a special criterion. The presence of macro- to micro-sized cracks in the material and the step structure of the cracking process create prerequisites for effective dispersed fiber reinforcement of the material [4]. Under the influence of external load in the composite material, the destruction of the process structure is initiated, which is expressed in the development of the first microcracks in the branching region. At the mouths of cracks, at the same time, a critical energy reserve is released, which entails further development of the microcrack network and leads to deterioration of the mechanical properties of the composite material [5].

In total, the given local fracture processes at the microscale level lead to the failure of the investigated sample, which provides a task for studying dispersed reinforcement of the material to improve crack resistance. Based on the hypothesis that dispersed-reinforcing fibers correspond in structure to cracks occurring at the meso-, macro-, and micro-levels of structural systems, it is recommended to develop a concrete mix composition taking into account multilevel reinforcement. Such an approach allows for providing increased resistance of the material to crack formation and propagation [6]. Despite significant progress, many studies focus on either the mechanical properties, chemical durability, or isolated effects of specific fibers without offering a systematic approach to combining multiple modifying agents. Some researchers explored microsilica and polymer fibers, yet did not fully assess their synergistic effects with basalt fibers.

It is worth noting that dispersed fillers should act as reinforcing elements at the microscale level, and elementary fibers at the macroscale level [7]. To investigate the influence of reinforcing elements on the crack resistance characteristic of heavy concrete, chopped basalt fiber and, for comparative analysis, polypropylene fiber were introduced into the concrete mix, which have proved themselves well [8].

The problem, therefore, lies in the lack of comprehensive research that integrates condensed microsilica suspension, modern plasticizers, and both micro- and macro-scale fibers to form a multiscale reinforcement system. There is a need to evaluate the combined effect of these modifiers under dynamic load conditions relevant to railway sleepers, where both fatigue resistance and crack control are critical. The goal of this research is to develop and investigate a modified heavy concrete mixture incorporating condensed microsilica suspension, a polycarboxylate-based plasticizer, and basalt fiber to improve crack resistance and mechanical properties under dynamic loading conditions, thus ensuring the structural durability of reinforced concrete sleepers.

2. Methods

In this research, Portland cement of the CEM I 42.5N grade, meeting the requirements of [9], was used as a binder. The cement was produced by ALACEM, LLP (Saryozek, Almaty region, Kazakhstan). The characteristics of the cement, provided by the factory testing laboratory, are presented in Tables 1 and 2.

Table 1 – Characteristics of Portland cement

Brand	Manufacturer	Chemical composition, % by weight						
		Na ₂ O	SO ₃	MgO	Fe ₂ O ₃	CaO	Al ₂ O ₃	SiO ₂
CEM I 42.5N	ALACEM, LLP	0.6	0.62	0.96	4.01	64.88	5.01	23.97

Table 2 – Mineral composition of Portland cement clinker

Brand	Mineral content in clinker, %			
	C ₄ AF	C ₃ A	C ₂ S	C ₃ S
CEM I 42.5N	10.24	6.87	12.77	60.94

An analysis of the presented data showed that the cement meets the required standards [9].

Natural sand from the Arna quarry (Arna village, Almaty region, Kazakhstan) was used as a fine aggregate. The properties of the sand were determined by [10] and are shown in Table 3.

Table 3 – Characteristics of sand

Manufacturer	True density, kg/m ³	Coarseness module	Bulk density, kg/m ³	Specific effective activity of natural radionuclides, Bq/kg	The content of clay and pulverized particles, %
LLP «Arna»	2595	2.46	1585	71.7	1.4

Based on the content of clay, fine impurities, and its granulometric composition, this sand meets the requirements of [11].

Granite crushed stone with a particle size ranging between 5 and 20 mm, produced by Kentas, LLP (Bayterek village, Almaty region, Kazakhstan) was used as the coarse aggregate. Its characteristics are presented in Table 4.

Table 4 – Test results of coarse aggregate

Manufacturer	Lamellar and needle-shaped grains, %	Pulverized, silty, and clay particles, %	Grade of crushed stone by crushing capacity	Frost resistance	Bulk density, kg/m ³	Specific effective activity of radionuclides, Bq/kg	The brand of rubble by abrasion
Kentas, LLP	12	0.89	1300	350	1380	85	I-1

The data in Table 4 confirm that the coarse aggregate meets the requirements of [12].

The superplasticizer "AR Premium" from ARGP, LLP (Astana, Kazakhstan) was used. According to its consumer properties, the "AR Premium" additive complies with the requirements of [13]. It is a superplasticizer based on polyoxyethylene derivatives of polycarboxylic acids. It is used in the production of concrete and reinforced concrete structures made from heavy and fine-grained concrete, either under normal curing conditions or using electric heating. It is also used in the manufacture of building mortars. The recommended dosage of "AR Premium" is 0.6–1.0% by weight of cement. Dosage must be carried out with an accuracy of $\pm 1\%$ of the calculated amount. The normalized physico-chemical properties of the additive are presented in Table 5.

Table 5 – Physico-chemical parameters of the superplasticizer

Appearance	Density at 20 °C, g/cm ³ , not less than	Hydrogen ion activity index (pH), not less than	Mass fraction of chlorine ions, %, not more than
Light brown aqueous solution	1.03	4.2	0.01

Condensed microsilica (MC-95), a pulverized industrial by-product produced by Tau Ken Temir, LLP (Karaganda, Kazakhstan), was used as a micro-filler. This microsilica obtained from ferrosilicon production via electrostatic precipitators has particle sizes ranging from 5 to 50 microns. Its qualitative characteristics are presented in Table 6.

Table 6 – Characteristics of MC-95 grade silica

Indicators	Qualitative characteristics
Mass fraction of silicon dioxide, %, not less (SiO ₂)	95.91
Mass fraction of phosphorus oxide (P ₂ O ₅), %, max	0.1
Mass fraction of magnesium oxide (MgO), %, max	0.6
Mass fraction of aluminum oxide (Al ₂ O ₃), %, max	0.16
Mass fraction of iron oxide (Fe ₂ O ₃), %, max	0.22
Mass fraction of sulfuric anhydride (SO ₃), %, max	0.41
Mass fraction of calcium oxide (CaO), %, max	0.37
Mass fraction of free alkalis (Na ₂ O, K ₂ O), %, max	1.55
Mass fraction of water, %, max	0.29

Analysis of data in Table 6 above confirms that the coarse aggregate meets the requirements of [14].

To improve crack resistance, micro-reinforcing components were introduced during the dry mixing stage of the binder (Portland cement) with the fine and coarse aggregates. These included chopped basalt fiber, produced according to [15], and polypropylene fiber, manufactured by “Damu-Khimiya” (Karaganda, Kazakhstan). The general appearance and physical-mechanical properties of the fibers are shown in Figure 1 and Table 7.

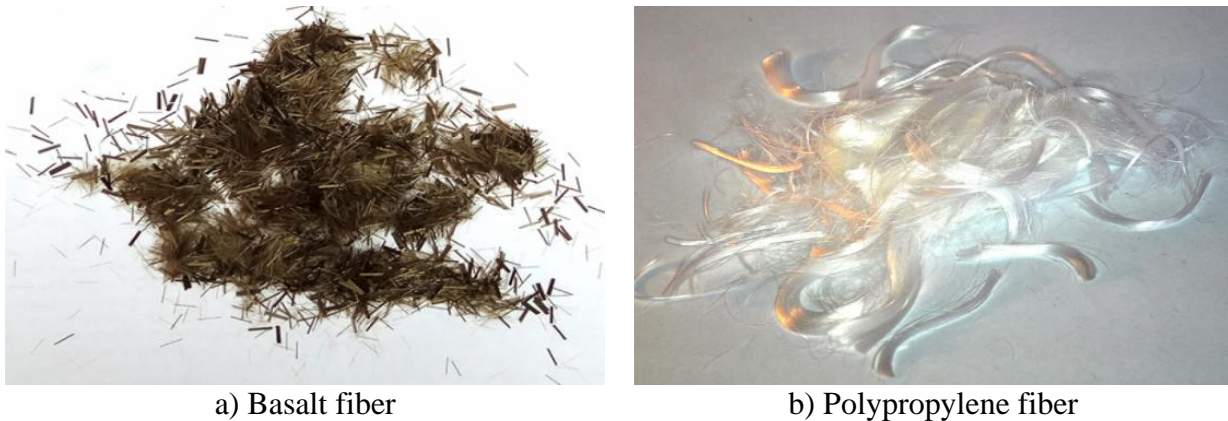


Figure 1 – Micro-reinforcing component

Table 7 – Physical and mechanical characteristics of basalt fiber and polypropylene fiber

Indicator	Characteristics	
	Basalt fiber	Polypropylene fiber
Melting point, °C	1350	170
Length of the segment, mm	10.77	11
Alkali and corrosion resistance	High	Medium
Diameter of the elementary fiber, microns	18,24	50
Elongation at break, %	1.5-3.8	25-36
Tensile strength, R, MPa·10 ³	2.7-3.6	0.78
Density, g/cm ³	2.51	0.97
Modulus of elasticity F _f , MPa·10 ³	90-95	4.8

The goal of improving both the strength and economic characteristics of the heavy concrete mix was achieved by optimizing its structural density through the introduction of active silica and by reducing bending moments via dispersed fiber reinforcement. This approach increases the stability of the composite.

Concrete compositions containing silica, micro-reinforcing fibers, and chemical admixtures, calculated using the absolute volume method [16], are listed in Table 8.

Table 8 – Studied compositions of modified heavy concrete

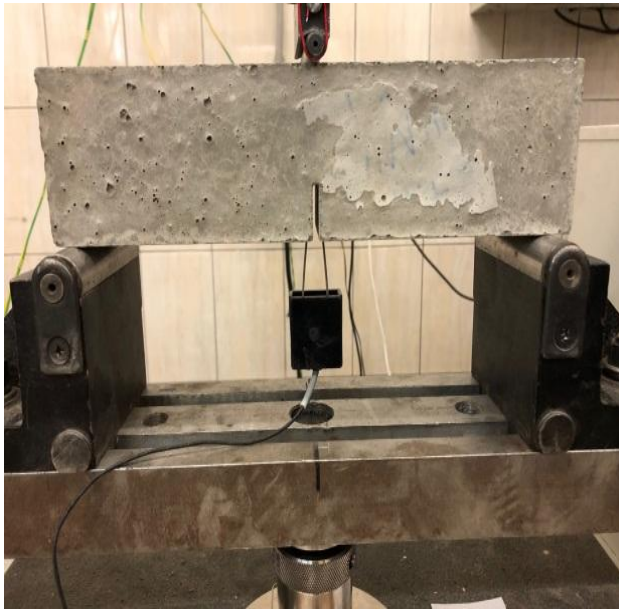
Materials	Composition and consumption per 1 m ³ of concrete mix, kg/m ³				
	No. 1 – Reference	No. 2 – 15% MG	No. 3 – 20% MG	No. 4 – 20% MG +0.75% BV	No. 5 – 20% MG +0.75% PF
CEM I 42.5N	420	357	336	336	336
Water	150	150	150	150	150
Granite rubble	1000	1000	1000	1000	1000
Sand	810	810	810	810	810
“AR premium” superplasticizer	4.2	4.2	4.2	4.2	4.2
Microsilica MCU-95	-	63	84	84	84
Basalt fiber (BF)	-	-	-	2.68	-
Polypropylene fiber (PPF)	-	-	-	-	2.68
In/C (C+MC)	0.36	0.36	0.36	0.36	0.36

According to the studies of Kaprielov S.S. and Sheinfeld A.V. [17], [18], the recommended silica content is 15–20% of the binder weight per 1 m³ of concrete. This range was adopted in the mix design. To determine the appropriate amount of MC-95 microsilica required for high-performance concrete, the additive was used in the same 15–20% range by binder weight.

The dosage and type of micro-reinforcing fiber were determined based on the works of Bazhenov Yu.M. and Mailyan L.R. [19], [20], where fiber lengths up to 12 mm and fiber content in the range of 0.5–1% by binder weight were recommended. The introduction of microsilica allowed for a reduction in cement consumption. This is due to its high reactivity, which leads to local clustering of cement particles during hydration. If not controlled, this can negatively affect the matrix structure. Economically, reducing cement content is also beneficial. According to [21], maintaining a distance between cement particles equal to the diameter of silica particles ensures uniformity and stability of the modified cement matrix.

The optimal composition of the combined admixture—including the high-range water-reducing "AR Premium" additive and MC-95 microsilica—was determined experimentally. For this, 100 × 100 × 100 mm cube samples were cast, cured under standard conditions for 28 days, and tested for strength characteristics.

To evaluate crack resistance under non-equilibrium loading, prism samples of size 70 × 70 × 280 mm were prepared, with four samples per mix, each featuring a 25 mm deep and 2 mm wide notch. Prior to testing, two loading/unloading cycles up to 10% of the expected load were performed. The samples were then continuously loaded (Figure 2a) until fracture (Figure 2b), at which point the load value F_c^* was recorded.



a) Sample before loading before testing



b) After loading

Figure 2 – Loading of a prism sample made of heavy modified concrete during the crack resistance test

The crack resistance characteristics of the prism samples are summarized in Table 9.

After testing, the crack resistance coefficient K_c^* was calculated using the following equation as proposed in [22]:

$$K_c^* = \frac{3F_c^* L_0}{2b^{1/2} t} \sqrt{a_0/b} (1.93 - 3.07\lambda + 14.53\lambda^2 - 25.11\lambda^3 + 25.8\lambda^4), \quad (1)$$

where: K_c^* – conditional stress intensity coefficient, [MPa·m^{0.5}]; F_c^* – load corresponding to the onset of crack propagation under dynamic testing, [MN]; b , t , L_0 , L , D – sample dimensions, [m]; a_0 – initial notch length, [m]; $\lambda = a_0/b$ – relative notch length; K_c^* – is the conditional stress intensity coefficient.

Table 9 – Characteristics of concrete samples for crack resistance testing

Marking of the sample	Sample number	Weight, g	Density, kg/m ³		Thickness at the incision site, mm
			ρ	ρ_{med}	
Composition 1 – Reference	1	3314.7	2416	2405.7	45.0
	2	3303.8	2408		45.0
	3	3294.2	2401		45.0
	4	3290.0	2398		45.0
Composition 2 – 15% MG	5	3298.3	2404	2403.2	45.0
	6	3302.4	2407		45.0
	7	3295.5	2402		45.0
	8	3292.8	2400		45.0
Composition 3 – 20% MG	9	3291.4	2399	2395.7	45.0
	10	3287.3	2396		45.0
	11	3283.2	2393		45.0
	12	3285.9	2395		45.0
Composition 4 – 20% MG +0.75% BV	13	3281.8	2392	2391.2	45.0
	14	3279.1	2390		45.0
	15	3276.3	2388		45.0
	16	3285.9	2395		45.0
Composition 5 – 20% MG +0.75% PF	17	3269.5	2383	2382.5	45.0
	18	3265.4	2380		45.0
	19	3266.7	2381		45.0
	20	3273.6	2386		45.0

3. Results and Discussion

For the reference sample (Composition 1), the values were: $F_c^* = 0.002086$ MN, $L_0 = 0.266$ m, $b=0.07$ m, $t=0.07$ m, $a_0=0.025$ m, $\lambda = 0.357143$, hence: $K_c^* = \frac{3 \cdot 0.002327 \cdot 0.266}{2 \cdot 0.07^2 \cdot 0.07} \cdot \sqrt{\frac{0.025}{0.07}} \cdot (1.93 - 3.07 \cdot 0.357143 + 14.53 \cdot 0.357143^2 - 25.11 \cdot 0.357143^3 + 25.8 \cdot 0.357143^4) = 0.052709$ MPa \times m^{0.5}.

Similarly, the conditional stress intensity factor K_c^* calculated for the remaining compositions:

- Composition 2 (15% MG): $F_c^* = 0.002201$ MN, $L_0 = 0.266$ m, $b=0.07$ m, $t=0.07$ m, $a_0=0.025$ m, $\lambda = 0.357143$, hence: $K_c^* = 0.055619$ MPa \times m^{0.5}.

- Composition 3 (20% MG): $F_c^* = 0.002328$ MN, $L_0 = 0.266$ m, $b=0.07$ m, $t=0.07$ m, $a_0=0.025$ m, $\lambda = 0.357143$, hence: $K_c^* = 0.058829$ MPa \times m^{0.5}.

- Composition 4 (20% MG+0.75% BV): $F_c^* = 0.002933$ MN, $L_0 = 0.266$ m, $b=0.07$ m, $t=0.07$ m, $a_0=0.025$ m, $\lambda = 0.357143$, hence: $K_c^* = 0.074122$ MPa \times m^{0.5}.

- Composition 5 (20% MG+0.75% PF): $F_c^* = 0.002741$ MN, $L_0 = 0.266$ m, $b=0.07$ m, $t=0.07$ m, $a_0=0.025$ m, $\lambda = 0.357143$, hence: $K_c^* = 0.069270$ MPa \times m^{0.5}.

Table 10 presents the maximum bending stress values, load, conditional stress intensity factor, and sample loading graphs, as shown in Figure 3.

Table 10 – Characteristics of crack resistance of samples during nonequilibrium tests

Marking of the sample	Load F_c^* , kN	Voltage, MPa	Indicator
			Conditional stress intensity coefficient K_c^* , MPa \times m ^{0.5}
Composition 1 – Reference	2.086	5.974	0.052709
Composition 2 – 15% MG	2.201	6.304	0.055619
Composition 3 – 20% MG	2.328	6.405	0.058829
Composition 4 – 20% MG +0.75% BV	2.933	8.064	0.074122
Composition 5 – 20% MG +0.75% PF	2.741	7.542	0.069270

An analysis of the results in Table 10 and the graphs in Figure 3 indicates that concrete samples modified with basalt fiber (composition 4) demonstrate improved performance. Specifically, the maximum load increased by 40.59%, the conditional stress intensity factor by 40.5%, and the bending stress by 40.49% compared to the reference composition without fiber reinforcement (composition 1).

Composition 4 also shows increases in maximum load, bending stress, and the conditional stress intensity factor by 7.1%, 6.93%, and 6.9%, respectively, compared to composition 5, which contains polypropylene fiber. Thus, the dispersed reinforcement of heavy concrete with basalt fiber enhances its physical and mechanical properties due to its positive effect on the concrete structure. An additional factor contributing to the structural strength of the concrete is microsilica, which promotes the binding of portlandite to form poorly soluble hydrosilicates. During crack resistance testing, stress redistribution occurs within the concrete and between the components of the cement matrix. This results in a reduction of stress concentration in areas of macrodefects, which limits the propagation and growth of major cracks. These findings are consistent with those of the study [23], which examined shrinkage in fiber-reinforced concrete with elementary fibers ranging from 6 to 18 mm in length. The data confirm increased adhesion between the cement-sand matrix and the basalt fibers added to the concrete mix, providing enhanced micro-reinforcement and enabling stress relaxation at the matrix–filler interface, outperforming polypropylene fiber in this regard. This conclusion aligns with the results of previous studies [24], [25].

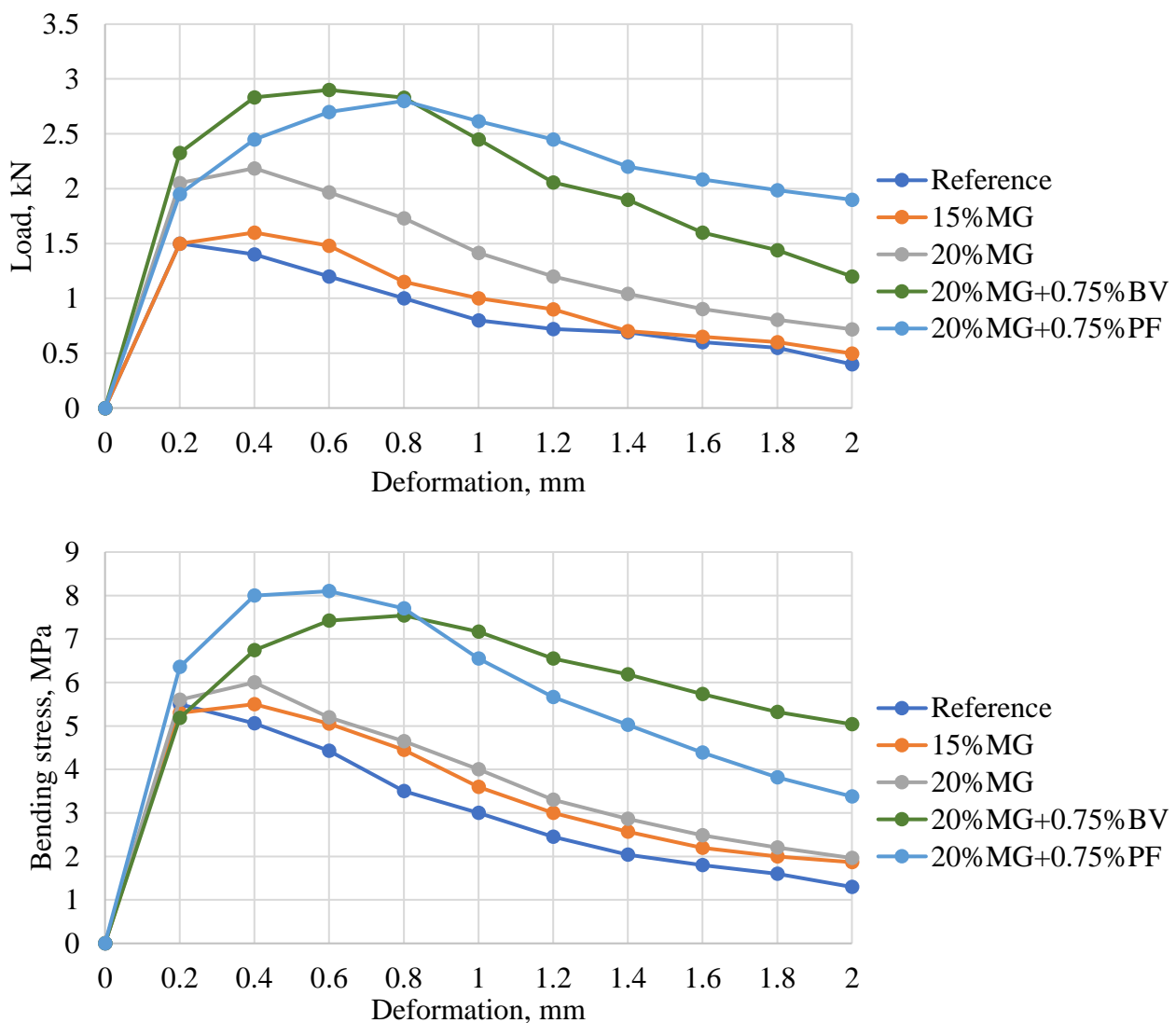


Figure 3 – Loading graphs of samples from modified heavy concrete

Analysis of Figure 3 shows that the prolonged crack opening behavior observed in samples of compositions 4 and 5 (reinforced with fibers) compared to the reference composition 1 (without fibers) indicates a high degree of fiber engagement during failure. The increased fracture toughness of the fiber-reinforced samples is characterized by relatively gradual descending branches in the load-deflection graphs for compositions 4 and 5.

Additionally, increased stress concentration along the micro-reinforcing fibers led to a marked difference in performance between compositions 1, 2, and 3 (without fibers) and compositions 4 and 5 (with micro-reinforcement), corroborating the findings reported in [19], [26].

4. Conclusions

The failure mechanisms and key crack resistance characteristics of the modified concrete samples were identified. Concrete samples containing basalt fiber (composition 4) exhibited increases in maximum load by 40.59%, the conditional stress intensity factor by 40.5%, and bending stress by 40.49% compared to the reference sample without fiber (composition 1). Furthermore, composition 4 demonstrated improvements of 7.1%, 6.93%, and 6.9% in maximum load, bending stress, and the conditional stress intensity factor, respectively, compared to composition 5 with polypropylene fiber. Therefore, dispersed reinforcement of heavy concrete with basalt fiber improves crack resistance due to its favorable impact on the concrete's internal structure. When evaluating crack resistance under prism loading, stress within the concrete is equalized and redistributed among the components of the cement matrix. This leads to a reduction in stress concentration near macrodefects, thereby limiting the development and propagation of primary cracks.

It has been established that the improved strength characteristics of modified heavy concrete compared to ordinary concrete are achieved through the introduction of high-performance fibers with a significantly higher modulus of elasticity than the concrete matrix and strong chemical resistance. The most effective approach is multiscale reinforcement, where microscale reinforcement is provided by highly dispersed fillers (e.g., silica) introduced along with cement, and macroscale reinforcement is achieved through fiber incorporation.

References

- [1] R. Chen, X. Zhao, Z. Wang, H. Jiang, and X. Bian, "Experimental study on dynamic load magnification factor for ballastless track-subgrade of high-speed railway," *Journal of Rock Mechanics and Geotechnical Engineering*, vol. 5, no. 4, pp. 306–311, Aug. 2013, doi: 10.1016/j.jrmge.2013.04.004.
- [2] *GOST 33320-2015 Reinforced concrete sleepers for railways. General technical conditions*. 2019.
- [3] M. Afroz, I. Patnaikuni, and S. Venkatesan, "Chemical durability and performance of modified basalt fiber in concrete medium," *Constr Build Mater*, vol. 154, pp. 191–203, Nov. 2017, doi: 10.1016/j.conbuildmat.2017.07.153.
- [4] C. J. Slebi-Acevedo, P. Lastra-González, P. Pascual-Muñoz, and D. Castro-Fresno, "Mechanical performance of fibers in hot mix asphalt: A review," *Constr Build Mater*, vol. 200, pp. 756–769, Mar. 2019, doi: 10.1016/j.conbuildmat.2018.12.171.
- [5] V. P. Sychev, D. V. Ovchinnikov, A. Yu. Abdurashitov, V. A. Pokatsky, and A. V. Sycheva, "Rails life cycle evaluation depending on the operating conditions," 2023, p. 020010. doi: 10.1063/5.0104545.
- [6] J. P. Romualdi and G. B. Batson, "Mechanics of crack arrest in concrete," in *American Concrete Institute, ACI Special Publication*, 2008. doi: 10.1061/jmcea3.0000381.
- [7] Y. Wang, S. Hu, and X. Sun, "Experimental investigation on the elastic modulus and fracture properties of basalt fiber-reinforced fly ash geopolymer concrete," *Constr Build Mater*, vol. 338, 2022, doi: 10.1016/j.conbuildmat.2022.127570.
- [8] D. A. Akhmetov *et al.*, "The Effect of Low-Modulus Plastic Fiber on the Physical and Technical Characteristics of Modified Heavy Concretes Based on Polycarboxylates and Microsilica," *Materials*, vol. 15, no. 7, p. 2648, Apr. 2022, doi: 10.3390/ma15072648.
- [9] *GOST 31108-2016 Cements for general construction. Technical conditions*. 2019.
- [10] *GOST 8735-88 Sand for construction works. Methods of testing*. 2018.
- [11] *GOST 8736-2014 Sand for construction works. Technical conditions*. 2019.
- [12] *GOST 8267-93 Crushed stone and gravel from dense rocks for construction works. Technical conditions*. 2018.

- [13] GOST 24211-2008 *Additives for concrete and mortars. General technical conditions*. 2010.
- [14] GOST 58894-2020 *Condensed microsilica for concrete and mortars. Technical conditions*. 2020.
- [15] TU 5952-002-13307094-08 *Chopped basalt fiber*. 2008.
- [16] Yu. M. Bazhenov, *Technology of concrete*. Moscow: ASV, 2011.
- [17] S. S. Kaprielov, A. V. Sheynfeld, I. A. Chilin, V. G. Dondukov, and N. M. Selyutin, "Modified concrete: reality and prospects," *Bulletin of Science and Research Center of Construction*, vol. 40, no. 1, pp. 92–104, Mar. 2024, doi: 10.37538/2224-9494-2024-1(40)-92-104.
- [18] S. S. Kaprielov, A. V. Sheynfeld, and G. S. Kardumyan, *New modified concretes*. Moscow: Paradis, 2010.
- [19] Yu. M. Bazhenov, B. C. Demyanova, and V. I. Kalashnikov, *Modified high quality concretes*. Moscow: Publishing House of the Association of Construction Universities, 2006.
- [20] L. R. Mailyan, S. A. Stelmakh, M. G. Kholodnyak, and E. M. Shcherban, "Selection of fiber types for dispersed reinforcement of products from centrifuged concrete," *Science (1979)*, vol. 9, no. 4, pp. 1–8, 2017.
- [21] T. A. Nizina and A. S. Balykov, "Experimental-statistical models of properties of modified fiber-reinforced fine-grained concretes," *Magazine of Civil Engineering*, vol. 62, no. 02, pp. 13–25, Sep. 2016, doi: 10.5862/MCE.62.2.
- [22] GOST 29167-91 *Concretes. Methods of determination of crack resistance characteristics (fracture toughness) under static loading*. 2004.
- [23] D. Akhmetov *et al.*, "Effect of low-modulus polypropylene fiber on physical and mechanical properties of self-compacting concrete," *Case Studies in Construction Materials*, vol. 16, p. e00814, Jun. 2022, doi: 10.1016/j.cscm.2021.e00814.
- [24] K. Attia, A. El Refai, and W. Alnahhal, "Flexural Behavior of Basalt Fiber-Reinforced Concrete Slab Strips with BFRP Bars: Experimental Testing and Numerical Simulation," *Journal of Composites for Construction*, vol. 24, no. 2, Apr. 2020, doi: 10.1061/(ASCE)CC.1943-5614.0001002.
- [25] R. V. Lesovik, S. V. Klyuyev, A. V. Klyuyev, A. V. Netrebenko, V. T. Yerofeyev, and A. V. Durachenko, "Fine-grain concrete reinforced by polypropylene fiber," *Res J Appl Sci*, vol. 10, no. 10, 2015, doi: 10.3923/rjasci.2015.624.628.
- [26] N. M. Morozov, N. M. Krasnikova, O. V. Khokhryakov, and V. G. Khozin, "Optimization of composition of cement concrete for airfield coverings," *Izv. Kazan State Univ. Archit. Civ. Eng.*, no. 2(28), pp. 166–172, 2014.

Information about authors:

Ilyas Abdraimov – PhD Student, Mukhtar Auezov South Kazakhstan Research University, Almaty, Kazakhstan, abdraimov_ilyas@mail.ru

Musa Kuttybay – PhD Student, Mukhtar Auezov South Kazakhstan Research University, Almaty, Kazakhstan, m_kuttybay@mail.ru

Ibrakhim Kasimov – Professor, Tashkent University of Architecture and Civil Engineering, Tashkent, Uzbekistan, ibrahimkasimov61@gmail.com

Mariya Sailygarayeva – PhD, Senior Lecturer, The Kazakh National Agrarian Research University, Almaty, Kazakhstan, mariya_23365@mail.ru

Vladislav Pak – Master Student, International University of Transportation and Humanities, Almaty, Kazakhstan, ariranggroup@gmail.com

Yerkyn Turarov – Master Student, International University of Transportation and Humanities, Almaty, Kazakhstan, zh.erkin@mail.ru

Author Contributions:

Abdraimov Ilyas – concept, methodology.

Musa Kuttybay – resources, data collection, testing.

Kasimov Ibrahim – modeling, analysis, visualization.

Sailygarayeva Mariya – interpretation, drafting, editing, funding acquisition.

Vladislav Pak – data collection.

Yerkyn Turarov – data collection.

Conflict of Interest: The authors declare no conflict of interest.

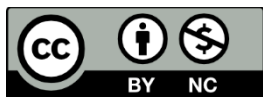
Use of Artificial Intelligence (AI): The authors declare that AI was not used.

Received: 08.02.2025

Revised: 21.05.2025

Accepted: 03.06.2025

Published: 04.06.2025



Copyright: @ 2025 by the authors. Licensee Technobius, LLP, Astana, Republic of Kazakhstan. This article is an open access article distributed under the terms and conditions of the Creative Commons Attribution (CC BY-NC 4.0) license (<https://creativecommons.org/licenses/by-nc/4.0/>).



Studying the material orthotropy effect under the plane stress state of triangular plates

Moldir Beketova¹, Zhmagul Nuguzhinov², Serik Akhmediyev¹, Valentin Mikhailov¹,
 Omirkhan Khabidolda^{3,*}

¹A.S. Saginov Karaganda Technical University, Karaganda, Kazakhstan

²Kazakhstan Multidisciplinary Institute of Reconstruction and Development (KazMIRR),
Karaganda, Kazakhstan

³E.A. Buketov Karaganda University, Karaganda, Kazakhstan

*Correspondence: oka-kargtu@mail.ru

Abstract. The article deals with the plane stress state of elastic thin orthotropic plates in the form of irregular triangles; orthotropy is assumed to be both physical and constructive. The research method used is the numerical finite difference method using a grid of scalene triangles. For such a grid, the authors have obtained resolving finite difference equations; in difference form they have obtained correct records of boundary conditions on the plate edges through the stress function based on the frame analogy taking into account the material orthotropy; typical finite difference equations are presented that allow solving problems of the plane stress state of triangular plates with a high degree of automation. As an illustrative example, a numerical calculation of triangular plates with a grid density of $N = 8$ is performed using a computer; the result of the study is the analysis of the stress state in the calculated grid nodes with a wide variation in the values of the lateral edges angles of inclination to the base of the triangle, the orthotropy coefficients. The results obtained demonstrate the feasibility and effectiveness of using a finite difference scheme on irregular triangular grids for analyzing the plane stress state of orthotropic plates. The developed approach provides a solid theoretical foundation for modeling stress distributions in structures with geometric and material anisotropy. The flexibility of the method allows adapting it to a wide range of boundary conditions and geometric configurations, laying the groundwork for further analytical development and integration into engineering software tools for structural analysis.

Keywords: triangular plate, versatile grid, material orthotropy, frame analogy, finite-difference equations, stress state of plates, asymmetry of the geometric pattern, loading in the plane, stress orthotropy.

1. Introduction

The object of the study is plates of complex geometric outline in the form of an irregular triangle with different angles at their apexes. Such structural elements are widely used in construction, transport, mechanical engineering, power engineering, aircraft, and shipbuilding. Triangular plates in construction are used as connecting elements for utilities, as supports for lateral reinforcement, and also during the assembly and installation of shelving units. They are used to secure items such as air ducts and cable trays. Studying their stress-strain state (SSS) is a rather complex technical problem due to the difficulty of satisfying the boundary conditions in the presence of oblique edges; at the same time, the problem is complicated by the heterogeneity of the structure of the materials used, in particular by their orthotropy the difference in elastic properties in mutually perpendicular directions [1]. A lot of works deal with studying orthotropic plates. Among them, there are works [2], [3], [4].

In this regard, in the presence of many methods of studying the stress-strain state of objects of mechanics of a deformable solid in the form of two-dimensional structures (plates), it is advisable to use the numerical finite difference method (FDM); in this case, it is desirable to use a two-dimensional grid of scalene triangles that rationally approximates the surface of the plates in the form

of an irregular triangle. However, in this case, there is a problem of recording the boundary conditions on the oblique edges in finite differences; such a problem does not arise when calculating rectangular plates using a rectangular grid.

The paper [5] discusses the development of six low-order triangular finite elements intended for the linear static analysis of both thick-walled and thin-walled shell structures. The authors propose a combination of two plane-stressed triangular elements with three bending triangular elements, which allows the formation of three-node shell elements with 18 degrees of freedom. The paper [6] considers the complex behavior of an elastic triangular plate supported by a one-sided Winkler foundation, with an emphasis on studying forced vibrations. The work covers both static and dynamic analysis, including the cases of uniformly distributed load and eccentrically applied concentrated force. To construct the basic mathematical model, the authors use the Chebyshev series to approximate the displacement functions and the Lagrange method to obtain the equations of motion. Taking into account the nonlinear characteristics of the one-sided foundation, a numerical iterative solution method is developed that allows an adequate description of the interaction of the plate with the foundation. In the paper [7], a mixed finite element method is considered for modeling the bending of thin plates within the Kirchhoff–Love theory. The proposed approach is based on the use of triangular and parallelogram meshes and includes the construction of low-dimensional local functional spaces, as well as the corresponding degrees of freedom. These spaces provide consistency with a sufficiently rich tensor space and allow the implementation of all physically justified Dirichlet and Neumann boundary conditions. The paper [8] presents a generalized approach to modeling thin plates and shells based on six different models formulated using three types of curvature operators defined in the moving coordinate system. These models are designed to describe both residually flat and residually curved triangular meshes, which is especially important when modeling complex deformable surfaces. The paper [9] presents an analytical construction of the rigidity matrix of a structural element based on the Sierpinski triangle under transverse bending conditions. The approach does not rely on classical integration over volume or surface but is based solely on fundamental principles: symmetry, balance, and self-similarity inherent in fractal structures. Due to a high degree of symmetry and recursive structure of the Sierpinski triangle, it is shown that the resulting rigidity matrix can be expressed through a single material parameter that reflects the mechanical properties of the material. This allows for significant simplification of both the theoretical description and the numerical implementation of the model. The paper [10] presents the development and analysis of a new triangular element for modeling the bending of thin plates, taking into account the transverse shear effect. The DSPM3 element is based on the improvement of the existing T3 γ r element and has three degrees of freedom at each corner node, which makes it convenient for implementation in numerical methods.

Three-dimensional structures in the form of triangular plates of small and medium thickness with isotropic and orthotropic characteristics of materials were considered in the work [11]. The finite difference method was used with a grid of scalene triangles. Based on a numerical algorithm and proprietary programs, the parameters were calculated for transverse and planar loading for various boundary conditions.

In the study [12], the bending behavior of elastic isotropic plates shaped as arbitrary triangles is considered under various types of boundary conditions, such as hinged or clamped (rigidly fixed) edges. In this case, the finite element method (FEM) is employed. As an illustrative example, the study presents the bending of a right-angled triangular plate with hinged support along its perimeter. In studies [13], [14], a calculation method based on the shape factor with the use of affine transformations is proposed for calculating triangular plates. The bending stress-strain state of the plates is considered, including cases of free vibrations. In this case, the plate material can be isotropic or orthotropic. In work [15], the finite element method is used to study free vibrations of thin isotropic triangular plates in the presence of a hole, with the edges being hinged and clamped. A comparison of the obtained results with the data of the experimental method is carried out, and the error was up to 6%. In work [16] a thin triangular plate of arbitrary shape is considered; for free vibrations the numerical method is used under complex boundary conditions, including that in the presence of

supports inside the plate region. In work [17], the analysis of vibration processes and multi-criteria optimization of a rigid triangular plate were performed. Structurally, the triangular plate included stiffeners located relative to one of its sides. The resolving equation for the transverse bending of the plate was obtained taking into account the effect of the orthotropy parameters and external disturbance. The initial differential equation of the system was obtained based on the Bubnov-Galerkin method. Then, multi-objective optimization was carried out taking into account two objective functions: the nonlinearity of the system and the amplitude of oscillations. There were considered the following interrelated parameters: the plate thickness, its geometry, and the distance between the stiffeners. The effect of the initial parameters on the optimal solutions and their distribution were also studied.

The force vibration in the plane of an arbitrary layered triangular plate with complex boundary conditions was studied by the Chebyshev-Ritz method in work [15]. The coordinate transformation allowed reducing the triangular layered plate of arbitrary shape to an equivalent square plate. After the transformation, the displacement functions of the square plate were expressed through two-dimensional Chebyshev polynomials with the corresponding coefficients. Arbitrary elastic boundary conditions were modeled by adjusting the stiffness of each spring using the method of conditional virtual springs. The characteristics of free vibrations of a triangular layered plate under various boundary conditions were calculated. Reliability of the method was confirmed by comparison with the results obtained by the finite element method, as well as with experimental data. The analysis showed that the proposed method had high convergence and sufficient calculation accuracy.

The bending of cantilever triangular plates with the same angles of inclination of the lateral faces to the base was studied in work [18]. The finite difference method was used for the analysis. The results obtained were combined to solve the problem of the acute angle effect at the top of the plate. The calculations of a cantilever beam with variable bending rigidity were compared with similar calculations of a triangular plate reinforced along the contour using a reduction factor. The theoretical provisions and practical results of this study can be partially applied to study the bending of orthotropic scaled triangular plates with reinforcement along the edges.

The frequencies and modes of free vibrations of thin isotropic triangular plates with a central hole were studied under various boundary conditions in work [19]. The finite element method was used for the analysis. The spectrum of vibration modes of some triangular plates was compared with similar characteristics of square plates with hinged and rigid edge fixation. The presented numerical values of natural frequencies and vibration modes of triangular plates showed good agreement with the experimental data.

For the analytical solution to the problem of free vibrations of regular triangular plates, the simplified superposition method was used in work [20]. The problem was solved by dividing it into three subproblems, which were solved by symplectic methods by imposing a separation of variables on the control equation based on the Hamiltonian system and a symplectic expansion in eigenvalues. Then, analytical solutions were obtained for the frequency and mode shape, requiring equivalence between the original problem and the superposition. Comparison with numerical results for regular triangular plates confirmed the convergence and accuracy of the approach. Thus, the analysis of scientific research in the field of triangular plates shows that, despite the wide range of boundary conditions under consideration, many authors avoid their calculations due to the complexity of the fastening conditions. The proposed calculation method will allow solving the future problems of the plane stress state of triangular plates with complex loading patterns along their contour.

The main goal and objectives of the study are as follows. The authors of the article developed a specialized program for calculating the plane stress state (with the grid density of $N=8$) with a high degree of automation that ensured the calculation of all the types of stress in the median plane. The main goal is also developing a numerical finite difference method using a grid of scalene triangles, including implementation of boundary conditions and the development of an algorithm for solving problems of the plane stress state.

2. Methods

Let us consider the plane stress state of triangular orthotropic plates under their all-round compression by a uniformly distributed load of intensity “q” (Figure 1); in the general case, it is accepted that $\alpha \neq \beta$.

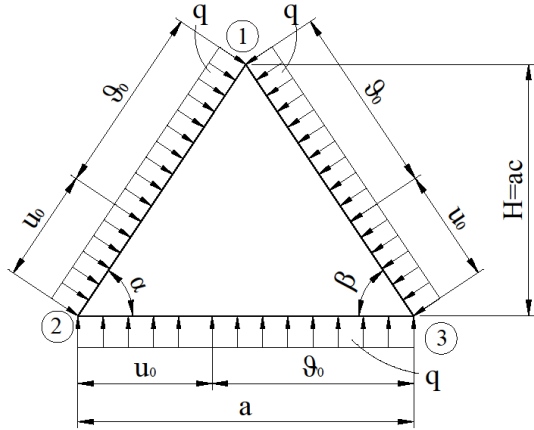


Figure 1 – Computational pattern of the plate

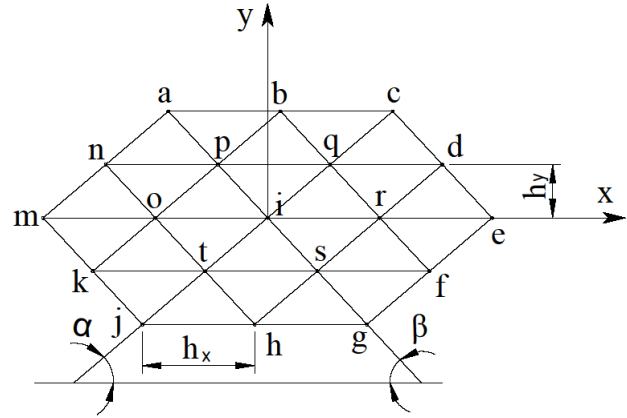


Figure 2 – Fragment of a grid of scalene triangles

The original fourth-order differential equation with variable coefficients has the form [21]:

$$\frac{\partial^4 F}{\partial x^4} + \alpha_0 \frac{\partial^4 F}{\partial x^2 \partial y^2} + \beta_0 \frac{\partial^4 F}{\partial y^4} = 0, \quad (1)$$

where $F=F(x, y)$ is the stress function. The orthotropy coefficients:

$$\alpha_0 = \frac{2a_{12} + a_{66}}{a_{22}} = E_2 \left(\frac{1}{G} - \frac{2\nu_2}{E_1} \right), \quad \beta_0 = \frac{a_{11}}{a_{22}} = \frac{E_2}{E_1} \quad (2)$$

Stresses in the midplane of the plates are expressed through the stress function "F", which is as follows:

$$\sigma_x = \frac{\partial^2 F}{\partial y^2}; \quad \sigma_y = \frac{\partial^2 F}{\partial x^2}; \quad \tau_{xy} = -\frac{\partial^2 F}{\partial x \partial y}. \quad (3)$$

The finite difference operators for the i -th node of the triangular grid included in equation (1) were obtained earlier [1].

Then equations (1) for the i -th node (Figure 2) will take the following form (without taking into account the boundary conditions):

$$\begin{aligned} & \psi_1 F_1 + \psi_2 (F_0 + F_r) + \psi_3 (F_p + F_s) + \psi_4 (F_q + F_t) + \psi_5 (F_n + F_f) + \psi_6 (F_b + F_h) + \\ & + \psi_7 (F_d + F_k) + \psi_8 (F_m + F_e) + \psi_9 (F_a + F_g) + \psi_{10} (F_c + F_y) = 0, \end{aligned} \quad (4)$$

where:

$$\begin{aligned} \psi_1 &= 6C^4 + \alpha_0 C^2 (-6AB + 4) + \beta_0 [4(AB - 1)^2 + 2(AB)^2 + 2A^2 + 2B^2], \\ \psi_2 &= -4C^4 + \alpha_0 C^2 (4AB - 2) + \beta_0 [-4AB(AB - 1) + 2AB], \\ \psi_3 &= \alpha_0 C^2 (B - 2A) + \beta_0 [4A(AB - 1) - 2AB^2], \\ \psi_4 &= \alpha_0 C^2 (A - 2B) + \beta_0 [4B(AB - 1) - 2A^2 B], \\ \psi_5 &= \alpha_0 C^2 A - 2\beta_0 A^2 B; \quad \psi_6 = 2\beta_0 AB; \quad \psi_7 = \alpha_0 C^2 B - 2\beta_0 AB^2; \\ \psi_8 &= C^4 - \alpha_0 C^2 AB + \beta_0 (AB)^2; \quad \psi_9 = \beta_0 A^2; \quad \psi_{10} = \beta_0 B^2, \end{aligned} \quad (5)$$

here (the triangular grid parameters):

$$A = \frac{\sin \beta \cos \alpha}{\sin(\alpha + \beta)}; \quad B = \frac{\sin \alpha \cos \beta}{\sin(\alpha + \beta)}; \quad C = \frac{\sin \alpha \sin \beta}{\sin(\alpha + \beta)}; \quad (6)$$

$$U = C^2 - AB = -\frac{\sin \alpha \sin \beta \cos(\alpha + \beta)}{\sin^2(\alpha + \beta)}; \quad h_x = a / N; \quad h_y = h_x a.$$

where: N is the number of divisions of the triangle sides ("grid density").

With ($\alpha_0=2$; $\beta_0=1$), according to (4, 5) there is a special case of the plane stress state for isotropic triangular plates [1].

The boundary conditions along the edges of the plate (Figure 3) are also written in finite differences in the form of a frame analogy (taking into account the orthotropy of the material) [1], [21]:

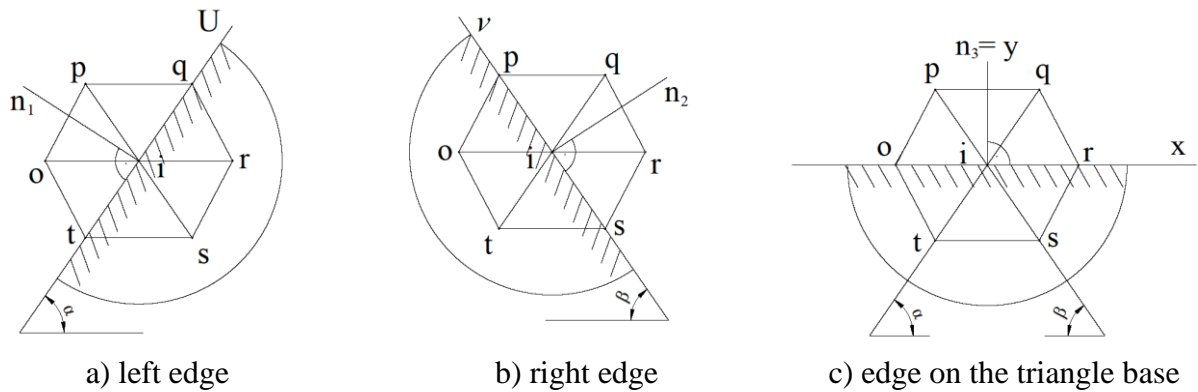


Figure 3 – Towards the boundary conditions

$$F_i = \pm M_i; \quad \partial F_i / \partial n_j = N_i \quad (j=1, 2, 3), \quad (7)$$

where (M_i , N_i) are nodal values of the bending moment and longitudinal force in the main system that is a statically determinate and geometrically unchangeable frame, the rods of which are the edges (sides) of a given triangular plate.

Expressions (7) will take the following form at the nodes of the triangular grid:

a) along the left edge (Figure 3a) ($j=1$):

$$(0.5\psi_5^* F_0 + \psi_9 F_p) = \frac{\sin \alpha}{2h_y \cdot C} (0.5\psi_5 F_r + \psi_9 F_s) + \frac{2h_y \cdot C}{\sin \alpha} (N_i) \quad (8)$$

b) along the right edge (Figure 3b) ($j=2$):

$$(0.5\psi_7 F_r + \psi_{10} F_q) = \frac{\sin \beta}{2h_y \cdot C} (0.5\psi_7 F_0 + \psi_{10} F_t) + \frac{2h_y \cdot C}{\sin \beta} (N_i); \quad (9)$$

c) along the triangle base (Figure 3c) ($j=3$):

$$(0.5\psi_6 F_s + \psi_{10} F_t) = \frac{1}{2h_y} (0.5\psi_6 + \psi_{10} F_q) + 2h_y (N_i). \quad (10)$$

Based on the main finite-difference equation (4), taking into account expressions (8-10), excluding the stress functions of the contour and edge nodes of the triangular grid, typical finite-difference equations are obtained for triangular plates at arbitrary values of the "oblique" angles α and β (Figure 1); the number of which is equal to seven (Figure 4): I - for intra-contour nodes; II - for grid nodes near the left edge (1-2); III - the same, near the right edge (1-3), IV - the same, near the edge (2-3), at the base of the triangle; V - at the apex of the triangle (1); VI - the same, at the apex (2); VII - the same, at the apex (3). The entry of typical finite-difference equations is given in Table 1.

Table 1 – Standard finite-difference equations of the plane stress state of orthotropic triangular plates

No.	i	o	r	p	s	q	t	n	f	b	h	d	k	m	e	a	g	c	j	right part
I	Ψ_1	Ψ_2	Ψ_2	Ψ_3	Ψ_3	Ψ_4	Ψ_4	Ψ_5	Ψ_5	Ψ_6	Ψ_6	Ψ_7	Ψ_7	Ψ_8	Ψ_8	Ψ_9	Ψ_9	Ψ_{10}	Ψ_{10}	P_I
II	$\Psi_1+(\Psi_8+\Psi_9)$		Ψ_2		Ψ_3	$\Psi_4+0.5\Psi_5$	$\Psi_4+0.5\Psi_5$	Ψ_5		Ψ_6	Ψ_7		Ψ_8	Ψ_8	Ψ_9	Ψ_9	Ψ_{10}	Ψ_{10}	Ψ_{10}	P_{II}
III	$\Psi_1+(\Psi_8+\Psi_{10})$	Ψ_2		$\Psi_3+0.5\Psi_4$	$\Psi_3+0.5\Psi_4$		Ψ_4	Ψ_5		Ψ_6	Ψ_7	Ψ_8	Ψ_8	Ψ_9	Ψ_9		Ψ_{10}	Ψ_{10}	Ψ_{10}	P_{III}
IV	$\Psi_1+(\Psi_8+\Psi_{10})$	$\Psi_2+0.5\Psi_6$	$\Psi_2+0.5\Psi_6$	Ψ_3		Ψ_4		Ψ_5		Ψ_6	Ψ_7	Ψ_8	Ψ_8	Ψ_9		Ψ_{10}			Ψ_{10}	P_{IV}
V	$\Psi_1+(2\Psi_8+\Psi_9+\Psi_{10})$				$\Psi_3+0.5\Psi_4$		$\Psi_4+0.5\Psi_5$			Ψ_6			Ψ_8	Ψ_9					Ψ_{10}	P_V
VI	$\Psi_1+(2\Psi_9+\Psi_8+\Psi_{10})$		$\Psi_2+0.5\Psi_6$			$\Psi_4+0.5\Psi_5$					Ψ_7		Ψ_8				Ψ_{10}			P_{VI}
VII	$\Psi_1+(2\Psi_{10}+\Psi_8+\Psi_9)$	$\Psi_2+0.5\Psi_6$		$\Psi_3+0.5\Psi_4$				Ψ_5					Ψ_8	Ψ_9						P_{VII}

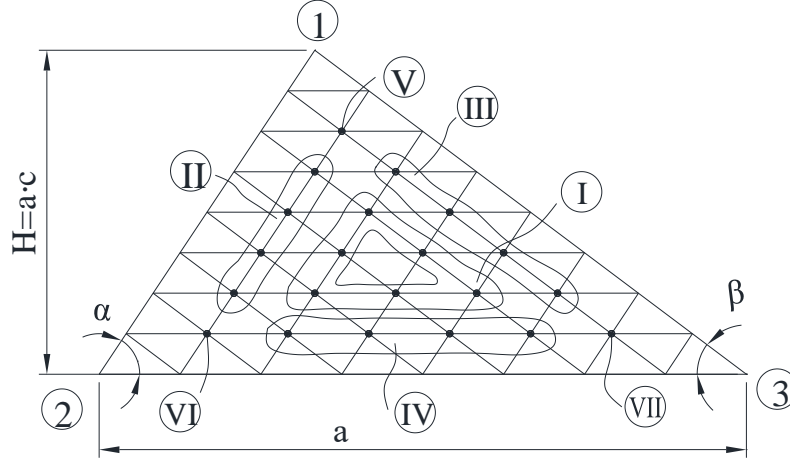


Figure 4 – Numbering of typical finite difference equations

The right parts of standard equations $P_i (i=1,2,...,7)$ are written as follows (Table 1):

$$\begin{aligned}
 P_I &= 0; \quad P_{II} = -(\psi_2 M_o + \psi_3 M_p + \psi_6 M_b + \psi_7 M_k) - \frac{2h_y C}{\sin \alpha} (N_o + N_p); \\
 P_{III} &= -(\psi_2 M_r + \psi_4 M_q + \psi_6 M_b + \psi_5 M_f) - \frac{2h_y C}{\sin \beta} (N_r + N_q); \\
 P_{IV} &= -(\psi_3 M_s + \psi_4 M_t + \psi_5 M_f + \psi_7 M_k) - 2h_y (N_t + N_s); \\
 P_V &= -(\psi_2 M_o + \psi_2 M_r + \psi_3 M_p + \psi_4 M_q + \psi_6 M_b + \psi_5 M_f + \psi_7 M_k) - \\
 &\quad - 2h_y C \left[\frac{1}{\sin \alpha} (N_o + N_p) + \frac{1}{\sin \beta} (N_r + N_q) \right]; \\
 P_{VI} &= -(\psi_2 M_o + \psi_3 M_p + \psi_7 M_k + \psi_4 M_t + \psi_3 M_s + \psi_5 M_f + \psi_6 M_b) - \\
 &\quad - 2h_y C \left[\frac{1}{\sin \alpha} (N_o + N_p) + (N_s + N_t) \right]; \\
 P_{VII} &= -(\psi_2 M_s + \psi_4 M_q + \psi_4 M_t + \psi_6 M_b + \psi_2 M_r + \psi_5 M_f + \psi_7 M_k) - \\
 &\quad - 2h_y C \left[\frac{1}{\sin \beta} (M_r + N_q) + (N_s + N_t) \right].
 \end{aligned} \tag{11}$$

Here (M_i, N_i) are nodal values of the bending moment and longitudinal force in a three-hinged contour frame (1-2-3) from a given compressive load “q” acting on the edges of the triangular plate (Figure 1).

To compare the obtained results, a study of the plane stress state for a triangular plate was conducted using the ANSYS program. The following parameters for orthotropic material were selected (Figure 5) and scheme of apply loads (Figure 6):

Properties of Outline Row 4: ortho			
	A	B	
1	Property	Value	
2	Material Field Variables	Table	
3	Orthotropic Elasticity		
4	Young's Modulus X direction	1,5E+11	Pa
5	Young's Modulus Y direction	3E+11	Pa
6	Young's Modulus Z direction	1E+11	Pa
7	Poisson's Ratio XY	0,1	
8	Poisson's Ratio YZ	0,2	
9	Poisson's Ratio XZ	0,1	
10	Shear Modulus XY	1,42E+10	Pa
11	Shear Modulus YZ	1E+10	Pa
12	Shear Modulus XZ	1E+10	Pa

Figure 5 – Orthotropic material properties

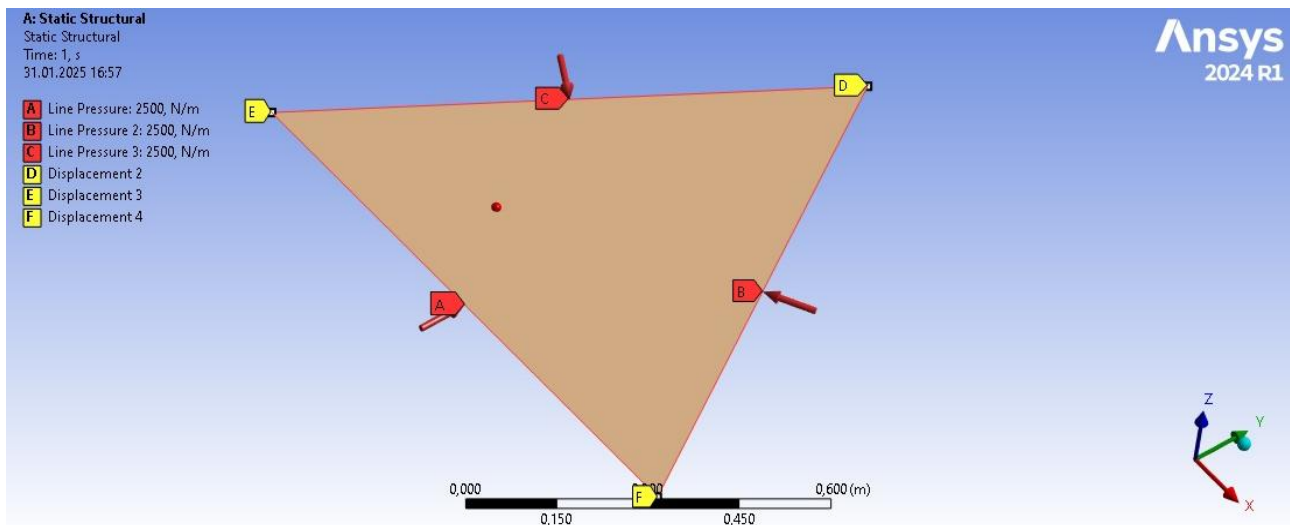


Figure 6 – Load parameters

3. Results and Discussion

The calculation algorithm when using the finite difference method for calculating the plane stress state of triangular plates is as follows [1], [4]. The surface of the plate is covered with a triangular grid with the number of divisions of its sides into "N" equal parts; Figure 7 shows the numbering of the calculated nodes of the grid from scalene triangles with the number of divisions of the sides $N=8$; here: (1, 2, ..., 21) is the numbering of the intra-contour grid nodes; (I, II, ..., XII) is the numbering of the grid nodes on the edges of the triangular plate.

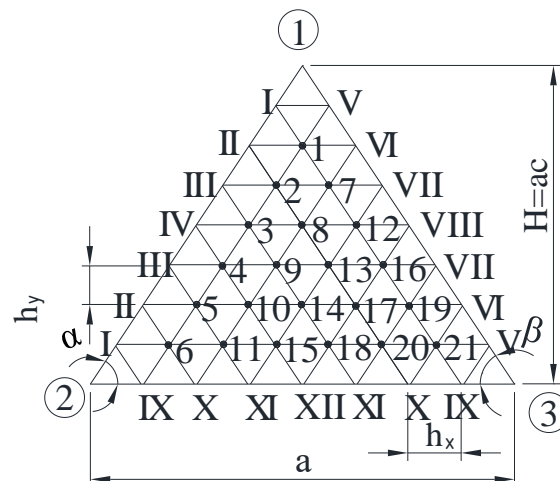


Figure 7 – Numbering of calculation nodes of the triangular grid

As a result of writing the finite difference equations (Table 1) for the calculated grid nodes (Figure 7), there is obtained a system of linear algebraic equations (SLAE) that has the following matrix form:

$$D \cdot \vec{F} = \vec{P}, \quad (12)$$

where \vec{F} is the vector of nodal values of stress functions; \vec{P} is the vector of the right part taking into account the load on the edges of triangular plates (formed in accordance with expressions (11)); D is the square matrix of the 21st order (Figure 7) that is formed from the values of the grid parameters in accordance with expressions (5).

The SLAE (12) solution gives the values of the vector \vec{F} :

$$\vec{F} = D^{-1} \cdot \vec{P}, \quad (13)$$

where D^{-1} is the inverse matrix.

Then, based on the values of vector \vec{F} (equation (13)) there are calculated stresses at the nodes of the triangular grid according to formulas (3):

1) for the grid nodes inside the plate contour (taking into account Figure 2):

$$\begin{aligned} \sigma_{xi} &= \frac{1}{h_y^2} [2(AB-1)F_i - AB(F_o + F_r) + A(F_p + F_s) + B(F_q + F_t)]; \\ \sigma_{yi} &= \frac{C^2}{h_y^2} (F_o - 2F_i + F_r); \\ \tau_{xy,i} &= \frac{C^2}{h_y^2} (2(A-B)F_i - (A-B)(F_o + F_r) + (F_q + F_t) - (F_p + F_s)). \end{aligned} \quad (14)$$

2) for the grid nodes at the edges of the plate

a) on left edge (1-2) (Figures 3, a and 4):

$$\begin{aligned} \sigma_{n_1} &= \frac{\partial^2 F}{\partial U^2} = \frac{\sin^2 \alpha}{h_y^2} (F_q - 2F_i + F_t); \\ \sigma_u &= \frac{\partial^2 F}{\partial n_1^2} = \frac{1}{h_y^2} \left\{ -2 \left(A + U + AU \frac{\sin^2 \alpha}{C^2} \right) F_i - \right. \\ &\quad \left. - AU \frac{\sin^2 \alpha}{C^2} (F_q + F_t) + 2[(UF_r + AF_s) + h_y N_i] \right\}, \\ \tau_{n_1, U} &= \frac{\partial^2 F}{\partial n, \partial u} = \frac{2C}{h_y^2} (N_q - 2N_i + N_t). \end{aligned} \quad (15)$$

b) on right edge (1-3) (Figures 3, b and 4):

$$\begin{aligned} \sigma_{n_2} &= \frac{\sin^2 \beta}{h_y^2} (F_p - 2F_i + F_s); \\ \sigma_g &= \frac{1}{h_y^2} \left\{ -2 \left(B + U + BU \frac{\sin^2 \beta}{C^2} \right) F_i - \right. \\ &\quad \left. - BU \frac{\sin^2 \alpha}{C^2} (F_p + F_s) + 2[(UF_o + BF_t) + h_y N_i] \right\}, \\ \tau_{n_1 r, g} &= \frac{\partial^2 F}{\partial n_2 \partial g} = \frac{2C}{h_y^2} (N_p - 2N_i + N_s). \end{aligned} \quad (16)$$

c) on edge (2-3) along the triangle base (Figure 3, c and 4):

$$\sigma_{xi} = \frac{1}{h_y^2} \left\{ 2(AB-1)F_i - AB(F_o + F_r) + 2 \left[(AF_p + BF_q) + h_y \cdot N_i \right] \right\};$$

$$\sigma_{yi} = \frac{C^2}{h_y^2} (F_o - 2F_i + F_r); \quad \tau_{xy,i} = \frac{\partial^2 F}{\partial x \partial y} = \frac{2C}{h_y^2} (N_o - 2N_i + N_r).$$
(17)

On the oblique edges of the triangular plate (1-2), (1-3) (Figure 4), the stress along their normal and tangential directions (n_i ($i=1, 2, u, v$)) is converted into stress along their Cartesian axes (x, y) using the following formulas:

a) at the nodes of left edge 1-2 (taking into account expressions (15)):

$$\sigma_x = \frac{0.5(\sigma_u - \sigma_{n_1}) \cos(2\alpha) + 0.5(\sigma_u + \sigma_{n_1}) \cos(4\alpha) - \tau_{n_1,u} \sin(2\alpha)}{\cos(4\alpha)};$$

$$\sigma_y = \frac{0.5(\sigma_u - \sigma_{n_1}) \cos(2\alpha) + 0.5(\sigma_u + \sigma_{n_1}) \cos(4\alpha) - \tau_{n_1,u} \sin(2\alpha)}{\cos(4\alpha)};$$

$$\tau_{xy} = - \frac{0.5 \left[\tau_{n_1,u} (2 \sin^2 \alpha - 1) + \sigma_u \sin(2\alpha) - \sigma_{n_1} \sin(2\alpha) \right]}{2 \sin^2(2\alpha) - 1};$$
(18)

b) at the nodes of right edge 1-3 (taking into account expressions (16)):

$$\sigma_x = \frac{0.5(\sigma_g - \sigma_{n_2}) \cos(2\beta) + 0.5(\sigma_g + \sigma_{n_2}) \cos(4\beta) - \tau_{n_2,g} \sin(2\beta)}{\cos(4\beta)};$$

$$\sigma_y = \frac{0.5(\sigma_g - \sigma_{n_2}) \cos(2\beta) + 0.5(\sigma_g + \sigma_{n_2}) \cos(4\beta) - \tau_{n_2,g} \sin(2\beta)}{\cos(4\beta)};$$

$$\tau_{xy} = - \frac{0.5 \left[2\tau_{n_2,g} (2 \sin^2 \beta - 1) + \sigma_g \sin(2\beta) + \tau_{n_2,u} \sin(2\beta) \right]}{2 \sin^2(2\beta) - 1}.$$
(19)

To illustrate the theory of calculating the plane stress state of triangular plates based on the finite difference method (FDM) proposed here, we will consider the results of calculating an equilateral ($\alpha=\beta=60^\circ$) orthotropic triangular plate under uniform compression along the perimeter with a load of intensity "q" (Figure 7). Tables 2 and 3 show the results of calculating the plane stress state of an equilateral ($\alpha=\beta=60^\circ$) orthotropic triangular (for the conventional material) plate with the material orthotropy coefficients $\alpha_0=1734$; $\beta_0=2.0$; (according to expressions (2)); $q=1000$ N/m.

Table 2 – Stresses in intra-contour nodes of orthotropic triangular plates

Grid node number (Figure 5)	Stresses, Pa ($\alpha=\beta=60^\circ$)					Stresses, Pa ($\alpha=45^\circ$; $\beta=60^\circ$)		
	$10^{-3}\sigma_{xi}$	$10^{-3}\sigma_{yi}$	$10^{-3}\tau_{xyi}$	Principal stresses		$10^{-3}\sigma_{xi}$	$10^{-3}\sigma_{yi}$	$10^{-3}\tau_{xyi}$
				$10^{-3}\sigma_1$	$10^{-3}\sigma_2$			
1	-1.034	-0.7161	0.00486	-0.0103	-1.7398	-0.7569	-0.2133	-0.416
2	-1.061	0.774	0.00634	-0.0523	-1.782	-0.60504	-0.54469	-0.1958
3	-1.04	-0.8423	0.0313	-0.0768	-1.806	-0.70168	-0.87142	-0.1929
4	0.975	-0.9374	-0.024	-0.0915	-1.821	-0.7299	-0.9884	-0.1432
5	-0.8287	-1.0159	-0.1483	-0.0575	-1.787	-0.74	-1.0347	-0.1147
6	-0.6256	-1.1154	-0.1943	-0.0087	-1.7353	-0.85567	-1.138	-0.1147
7	-1.049	-0.7488	-0.0046	-0.034	-1.7637	-0.8682	-0.4508	0.1238
8	-1.036	-0.6971	-0.0074	0.00188	-1.7314	-0.7111	-0.6438	-0.00205
9	-0.906	-0.7122	-0.175	-0.0555	-1.674	-0.711	-0.8243	-0.1489
10	-0.6894	-0.7705	-0.102	-0.1349	-1.594	-0.698	-0.9081	-0.19201
11	-0.3262	-0.7871	-0.2035	-9.3081	-1.421	-0.576	-0.8733	-0.19902
12	-1.041	-0.836	-0.026	-0.0748	-1.8037	-0.499	-0.5159	0.10643
13	-0.907	-0.7106	-0.1593	-0.0559	-1.6736	-0.7356	-0.6461	-0.00202
14	-0.6354	-0.7549	-0.0042	-0.1696	-1.556	-0.725	-0.8547	-0.00902
15	-0.3092	-0.8879	-0.0788	-0.266	-1.4631	-0.692	-0.9677	-0.1056
16	-0.9756	-0.9364	-0.022	-0.0913	-1.821	-0.8026	-0.8413	0.21903
17	-0.6899	-0.7698	-0.1018	0.1849	-1.5946	-0.776	-0.7669	-0.12471

18	-0.3094	-0.8874	-0.0707	0.2664	-1.4631	-0.7607	-0.9421	0.00356
19	-0.8288	-2.0159	0.0152	-0.0576	-1.7871	-0.8247	-1.0015	0.18969
20	-0.3264	-0.787	0.2035	0.30805	-1.4215	-0.7079	-0.8608	0.17969
21	-0.6256	-1.1154	0.1944	-0.0576	-1.7352	-0.8179	-1.0628	0.2117

Note: $\alpha_0=1,734$; $\beta_0=2,0$; $(q=1000 \text{ H/M}) = \text{const}$

Table 3 – Stresses on the edges (contour nodes) of an equilateral orthotropic triangular plate

Stresses ($10^{-3} \sigma_{ni}$; $10^{-3} \tau_{niui}$) at the grid nodes (Figure 5)												
On the left edge				On the right edge				On the triangle base				
	I	II	III	IV	V	VI	VII	VIII	IX	X	XI	XII
σ_{n1}	-1.0	-1.0	-1.0	-1.0	-	-	-	-	-	-	-	-
σ_u	-5.8556	-9.5018	-11.727	-12.549	-	-	-	-	-	-	-	-
τ_{n1u}		0.0			-	-	-	-	-	-	-	-
σ_{n2}	-	-	-	-	-1.0	-1.0	-1.0	-1.0	-	-	-	-
σ_v	-	-	-	-	-5.947	-9.729	-11.918	-12.554	-	-	-	-
τ_{n2v}	-	-	-	-		0.0						
$\sigma_{n3}(\sigma_y)$	-	-	-	-	-	-	-	-	-1.0	-1.0	-1.0	-1.0
σ_x	-	-	-	-	-	-	-	-	-1.28	-1.994	-2.578	-2.728
τ_{n3x}	-	-	-	-	-	-	-	-		0.0		

Figures 8 and 9 show the stress diagrams σ_{xi} (along section I-1-7-14-XII) and σ_{yi} (along section 2-IX-X-XI-XII; taking into account symmetry).

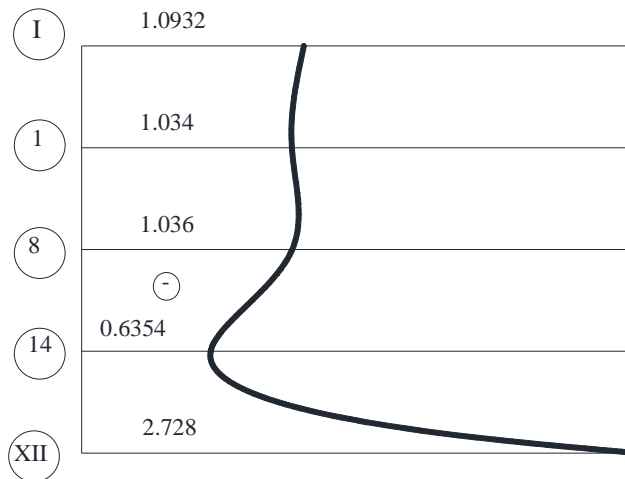


Figure 8 – Stress curve ($\sigma_{xi} 10^{-3}$, Pa [over section (I-1-8-14-XII)])

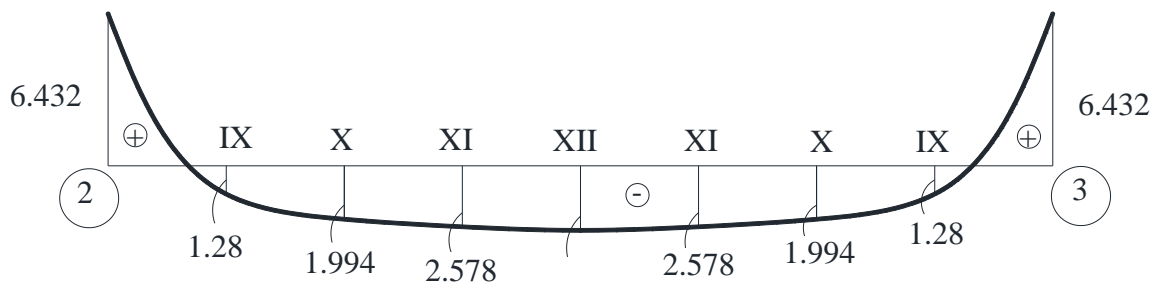


Figure 9 – Stress curve ($\sigma_{yi} 10^{-3}$, Pa) (over section (2-IX-X-XI-XII))

Tables 4 and 5 show the stress values at the grid nodes (Figure 7) depending on changing the angles α and β , as well as changing the orthotropy coefficients α_0 , β_0 ; Figures 10 and 11 show graphic images depending on these values.

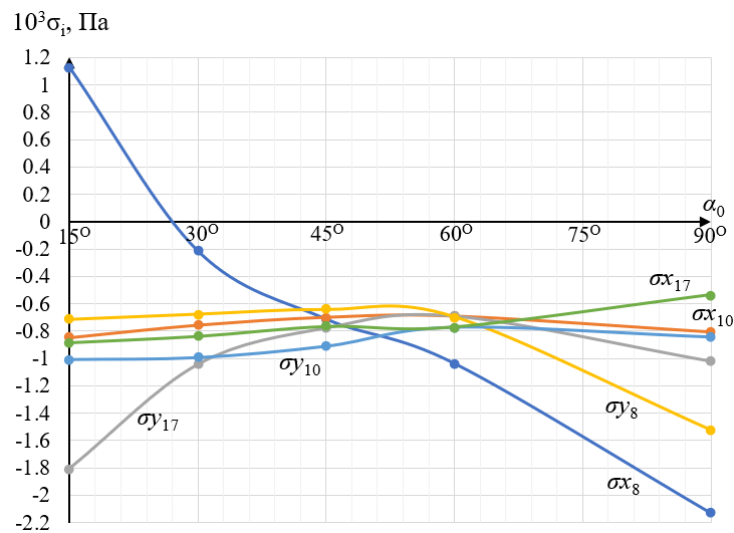
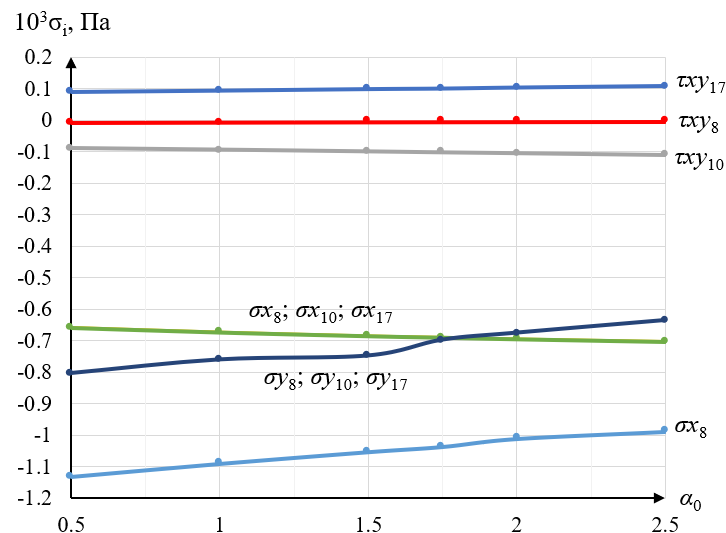
Table 4 – Stress dependence on the angles α and β

Values of the α angle	Other constant parameters	Current stresses, Pa									Principal stresses, Pa					
		$(\sigma_{x_i}) \cdot 10^{-3}$			$(\sigma_{y_i}) \cdot 10^{-3}$			$(\tau_{xy,i}) \cdot 10^{-3}$			$(\sigma_{1,i}) \cdot 10^{-3}$			$(\sigma_{2,i}) \cdot 10^{-3}$		
		i=8	10	17	8	10	17	8	10	17	8	10	17	8	10	17
15°	$\beta=60^\circ=\text{const};$ $\alpha_0=1,34;$ $\beta_0=2.0$ (q = 1000 N/m) = const.	1.13	-0.85	-1.81	-0.72	-1.00	-0.89	-0.24	-0.10	0.12	4.22	5.09	2.67	-3.81	-4.97	-5.35
30°		-0.21	-0.75	-1.04	-0.68	-0.99	-0.84	-0.14	-0.18	0.08	0.97	0.54	0.48	-1.86	-2.29	-2.36
45°		-0.71	-0.7	-0.78	-0.64	-0.91	-0.77	0	-0.19	0.17	0.18	0.06	0.09	-1.54	-1.66	-1.63
60°		-1.03	-0.69	-0.69	-0.70	-0.77	-0.77	0	-0.10	0.10	0	0.14	0.14	-1.73	-1.59	-1.59
90°		-2.13	-0.8	-1.02	-1.52	-0.84	-0.54	-0.26	0.29	-0.28	0.42	1.42	1.46	-4.07	-3.07	-3.02

Table 5 – Stress dependence on the orthotropy coefficients

Values of α_0	Other constant parameters	Current stresses, Pa									Principal stresses, Pa					
		$(\sigma_{x_i}) \cdot 10^{-3}$			$(\sigma_{y_i}) \cdot 10^{-3}$			$(\tau_{xy,i}) \cdot 10^{-3}$			$(\sigma_{1,i}) \cdot 10^{-3}$			$(\sigma_{2,i}) \cdot 10^{-3}$		
		i=8	10	17	8	10	17	8	10	17	8	10	17	8	10	17
0.5	$(\alpha=\beta=60^\circ)=\text{const};$ $\beta_0=2.0$ (q = 1000 N/m) = const.	-1.13	-0.66	-0.66	-0.20	-0.80	-0.79	0	-0.09	0.09	0.05	0.19	0.14	-1.88	-1.64	-1.64
1.0		-1.09	-0.67	-0.67	-0.76	-0.79	-0.79	-0.09	0.09	-0.04	0.15	0.15	0.15	-1.80	-1.61	-1.61
1.5		-0.05	-0.68	-0.68	-0.76	-0.78	-0.77	0	-0.10	0.10	0	0.14	0.14	-1.75	-1.60	-1.60
1.73		-1.04	-0.69	-0.69	-0.70	-0.77	-0.77	0	-0.10	0.10	0	0.13	0.13	-1.73	-1.59	-1.59
2.0		-1.02	-0.69	-0.69	-0.68	-0.77	-0.76	0	-0.10	0.10	0.02	0.14	0.14	-1.71	-1.59	-1.59
2.5		-1.99	-0.70	-0.70	-0.64	-0.76	-0.75	0	-0.11	0.11	0.06	0.14	0.14	-1.68	-1.60	-1.60

Figures 10 and 11 show the graphical dependencies of the stresses at the design point $i=8$ (Figure 7) with a change in the value of the angles α and β , as well as with a variation in the orthotropy parameters α_0 , β_0 .

Figure 10 – Stresses $(\sigma_{x_i}, \sigma_{y_i})$ dependence on the α angle ($\beta=60^\circ=\text{const}$)Figure 11 – Stresses $(\sigma_{x_i}, \sigma_{y_i})$ dependence on the orthotropy coefficients of α_0 ($\beta_0=2.0=\text{const}$)

To assess reliability of the results obtained by the authors that confirm the above theoretical positions, an alternative calculation of an equilateral orthotropic triangular plate was performed with the same initial data; the obtained pattern and values of stresses of the plane stress state are quite close (Figure 12, Table 6 in [21]) to those given in Tables 2 and 3.

In the course of the study, a comparative evaluation of the stress-strain state (SS) of a triangular plate under plane stress state was carried out using two numerical methods: the finite difference method (FDM) and the finite element method (FEM) implemented in the ANSYS software environment. Comparison of stress distribution in the fields of normal stresses σ_x , σ_y , and tangential stresses τ_{xy} obtained by both methods shows a qualitatively similar distribution pattern (Figure 12). The highest stresses are observed in the areas of load concentration and geometric features, which is consistent with the expected physical patterns. The stress values obtained at the nodal points show good quantitative agreement. The maximum relative error between the results does not exceed 2%, indicating good convergence of the solutions despite different numerical approaches.

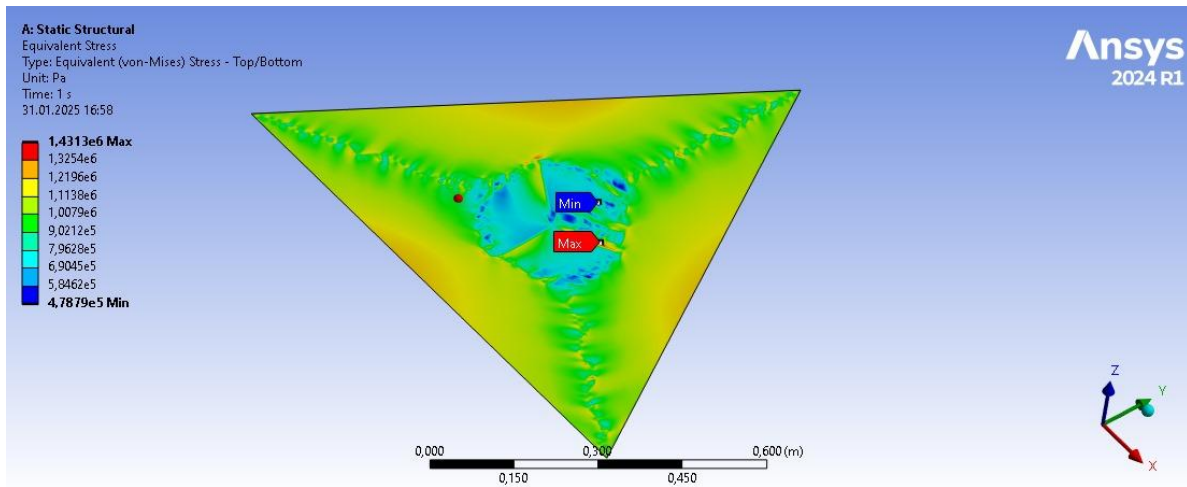


Figure 12 – Equivalent stresses

The finite difference method proved to be quite accurate for relatively simple triangular geometry and regular mesh, but its application becomes difficult for complex boundary conditions. In contrast, the finite element method in ANSYS is more flexible in constructing the computational model, especially in the presence of arbitrary geometry and inhomogeneous loading conditions.

Nevertheless, with adequate discretization and consideration of boundary conditions, the FEM is capable of producing results close to those obtained in ANSYS. This emphasizes the practical applicability of ICR in engineering analysis problems, especially in conditions of limited computational resources.

4. Conclusions

1. In this study, the plane stress state of orthotropic triangular plates was analyzed using the numerical finite difference method (FDM) based on a grid of scalene triangles. The results obtained allow drawing a number of important conclusions that can be useful both for further scientific research and for practical application in the design of thin-walled structures.

2. Using the well-known FDM procedure, resolving finite difference equations were obtained that took into account the plate geometry (angles α and β), orthotropic properties of materials (coefficients α_0 and β_0), loading in the midplane in the form of a plate distributed over part of the edges (parameters u_0 , v_0 (Figure 1)).

3. The recording of boundary conditions is shown based on the analogy for a grid of scalene triangles in accordance with the idea of pairwise exclusion of stress functions in the contour and edge nodes of the grid (expressions 8-10); here there are also given typical finite-difference equations near

the edges and at the apexes of a triangular plate (Table 1) which allows solving problems of the plane stress state for arbitrary values of the "oblique" angles (α and β) of the lateral edges of the plate.

4. Finite-difference equations of stresses (σ_x , σ_y , τ_{xy}) in the median plane for a grid of scalene triangles (including the nodes located on the edges of the plates) were obtained.

5. The authors of the article developed a special program for calculating the plane stress state (with the grid density of $N=8$) with a height of degree of automation for calculating all the types of stress in the median plane.

6. Using this program, a number of research problems were solved with variable parameters α and β ; α_0 and β_0 ; u_0 and v_0 ; they are presented in tabular and graphical forms.

7. The following was established:

a) for orthotropic equilateral triangular plates ($\alpha=\beta=60^\circ$), the stresses at the grid nodes will be symmetrical only in the direction of one median (to the base of the triangle); while for isotropic triangular plates, there are three axes of elastic symmetry (along all three medians);

b) for the diagrams in Figures 8, 9 the known conditions of equilibrium of external and internal forces are fulfilled, when the area of the diagrams (σ_x and σ_y) in different directions is equal to the resultant of external forces in the same directions, which indirectly confirms the reliability of the theoretical positions and results presented by the authors;

c) for orthotropic triangular plates, even under uniform compression along the perimeter, there is a non-uniform stress state (compared to similar isotropic triangular plates);

d) the following patterns can be traced in Figures 10, 11: the highest stress (σ_{x17}) occurs at $\alpha=45^\circ$; $\beta=60^\circ$ (Figure 10); at ($\alpha=\beta=60^\circ$) all the stress values (σ_{x8} , σ_{x10} , σ_{x17} , σ_{y8} , σ_{y10} , σ_{y17}) are close to each other as established based on the graphs and tables provided. The effect of the orthotropy coefficients on the stress values σ_{xi} , σ_{yi} turned out to be insignificant.

8. To verify the reliability of the obtained results, an alternative calculation was performed in the ANSYS program. The results obtained using the FDM turned out to be quite close to the data obtained in ANSYS, which confirmed the correctness of the proposed method and its applicability for solving problems of the plane stress state of orthotropic triangular plates.

9. The presented theoretical provisions and numerical results of the plane stress state of orthotropic triangular plates can serve as a basis for subsequent research into the stability problems of orthotropic triangular plates under non-uniform stress conditions.

10. The algorithm for calculating the plane stress state of orthotropic triangular plates proposed by the authors of this work can be widely used both in research problems of solid mechanics and in the practical design of thin-walled structures used as load-bearing elements of various buildings, engineering structures, mechanisms, and machines.

References

- [1] S. K. Akhmediyev, *Calculation of triangular plates*. Karaganda: KSTU, 2006.
- [2] M. Eröz, "Stress analysis of a pre-stretched orthotropic plate with finite dimensions," *Transactions of the Canadian Society for Mechanical Engineering*, vol. 45, no. 2, pp. 346–354, Jun. 2021, doi: 10.1139/tcsme-2019-0241.
- [3] Y. Xu and Z. Wu, "Exact solutions for rectangular anisotropic plates with four clamped edges," *Mechanics of Advanced Materials and Structures*, vol. 29, no. 12, pp. 1756–1768, May 2022, doi: 10.1080/15376494.2020.1838007.
- [4] Q. Yu, "A hierarchical wavelet method for nonlinear bending of materially and geometrically anisotropic thin plate," *Commun Nonlinear Sci Numer Simul*, vol. 92, p. 105498, Jan. 2021, doi: 10.1016/j.cnsns.2020.105498.
- [5] J. Petrolito and D. Ionescu, "Alternative Low-Order Triangular Elements for Thick and Thin Shell Analysis," *Int J Comput Methods*, vol. 22, no. 03, Apr. 2025, doi: 10.1142/S0219876223420069.
- [6] Z. Celep, Z. Özcan, and A. Güner, "Elastic triangular plate dynamics on unilateral Winkler foundation: Analysis using Chebyshev polynomial expansion for forced vibrations," *Journal of Mechanical Science and Technology*, vol. 39, no. 1, pp. 65–79, Jan. 2025, doi: 10.1007/s12206-024-1207-5.
- [7] T. Führer and N. Heuer, "Mixed finite elements for Kirchhoff–Love plate bending," *Math Comput*, Jul. 2024, doi: 10.1090/mcom/3995.
- [8] Q. Liang, "Corotational Hinge-based Thin Plates/Shells," *Computer Graphics Forum*, Apr. 2025, doi: 10.1111/cgf.70022.
- [9] M. Epstein and P. Vernon, "A triangular fractal plate bending element," *Zeitschrift für angewandte Mathematik und Physik*, vol. 75, no. 5, p. 163, Oct. 2024, doi: 10.1007/s00033-024-02300-0.

- [10] A. M. Katili, K.-U. Bletzinger, and I. Katili, "An optimum triangular plate element based on DSPM with incomplete quadratic functions and an assumed orthogonality condition," *Comput Struct*, vol. 296, p. 107301, Jun. 2024, doi: 10.1016/j.compstruc.2024.107301.
- [11] S. K. Akhmediyev, M. Y. Zhakibekov, I. A. Kurokhtina, and Z. S. Nuguzhinov, "Numerical study of stressed and strained state of thin walled structure of triangular plate type of small and middle thickness," *Structural Mechanics and Analysis of Constructions*, no. 2, pp. 28–33, 2015.
- [12] A. V. KOROBKO, N. G. KALASHNIKOVA, and E. G. ABASHIN, "Transverse bending and free vibrations of elastic isotropic plates in the form of isosceles triangles," *Building and reconstruction*, vol. 98, no. 6, pp. 20–27, 2021, doi: 10.33979/2073-7416-2021-98-6-20-27.
- [13] V. Korobko and S. Savin, "Free vibration of the triangular orthotropic plate with homogeneous and combined boundary conditions," *Building and reconstruction*, vol. 46, no. 2, pp. 33–40, 2013.
- [14] M. S. Beketova *et al.*, "Bending of orthotropic scalene triangle plates: finite difference modeling," *Magazine of Civil Engineering*, vol. 17, no. 7, p. 13407, 2025, doi: 10.34910/MCE.134.7.
- [15] O. Ya. Grigorenko, M. Yu. Borisenko, O. V. Boichuk, and L. Ya. Vasil'eva, "Free Vibrations of Triangular Plates with a Hole*," *International Applied Mechanics*, vol. 57, no. 5, pp. 534–542, Sep. 2021, doi: 10.1007/s10778-021-01104-3.
- [16] D. Cai, X. Wang, and G. Zhou, "Static and free vibration analysis of thin arbitrary-shaped triangular plates under various boundary and internal supports," *Thin-Walled Structures*, vol. 162, p. 107592, May 2021, doi: 10.1016/j.tws.2021.107592.
- [17] M. Sathyamoorthy, "Effects of large amplitude and transverse shear on vibrations of triangular plates," *J Sound Vib*, vol. 100, no. 3, pp. 383–391, Jun. 1985, doi: 10.1016/0022-460X(85)90294-9.
- [18] D. He, T. Liu, B. Qin, Q. Wang, Z. Zhai, and D. Shi, "In-plane modal studies of arbitrary laminated triangular plates with elastic boundary constraints by the Chebyshev-Ritz approach," *Compos Struct*, vol. 271, p. 114138, Sep. 2021, doi: 10.1016/j.compstruct.2021.114138.
- [19] S. K. Akhmediyev, O. Khabidolda, N. I. Vatin, G. A. Yessenbayeva, and R. Muratkhan, "Physical and mechanical state of cantilever triangular plates," *Journal of Mathematics, Mechanics and Computer Science*, vol. 118, no. 2, pp. 64–73, Jul. 2023, doi: 10.26577/JMMCS.2023.v118.i2.07.
- [20] Y. Yang, D. An, H. Xu, P. Li, B. Wang, and R. Li, "On the symplectic superposition method for analytic free vibration solutions of right triangular plates," *Archive of Applied Mechanics*, vol. 91, no. 1, pp. 187–203, Jan. 2021, doi: 10.1007/s00419-020-01763-7.
- [21] Varvak. P.M. and Varvak. L.P., *Method of grids in calculations of building structures*. Moscow: Stroyizdat, 1977.

Information about authors:

Moldir Beketova – PhD Student, A.S. Saginov Karaganda Technical University, Karaganda, Kazakhstan, moldir-9292@mail.ru

Zhmagul Nuguzhinov – Dr. Eng., Professor, Director of the Kazakhstan Multidisciplinary Institute of Reconstruction and Development (KazMIRR), Karaganda, Kazakhstan, kazmirr@mail.ru

Serik Akhmediyev – Candidate of Technical Sciences, Professor, A.S. Saginov Karaganda Technical University, Karaganda, Kazakhstan, serik.akhmediyev@mail.ru

Valentin Mikhailov – Candidate of Technical Sciences, Associate Professor, A.S. Saginov Karaganda Technical University, Karaganda, Kazakhstan, v.mihaylov@kstu.kz

Omirkhan Khabidolda – PhD, E.A. Buketov Karaganda University, Karaganda, Kazakhstan, okakargtu@mail.ru

Author Contributions:

Moldir Beketova – data collection, visualization, drafting.

Zhmagul Nuguzhinov – editing, testing, modeling, drafting.

Serik Akhmediyev – methodology, resources, analysis.

Valentin Mikhailov – analysis, interpretation, modeling.

Omirkhan Khabidolda – interpretation, modeling, methodology

Conflict of Interest: The authors declare no conflict of interest.

Use of Artificial Intelligence (AI): The authors declare that AI was not used.

Received: 03.03.2025

Revised: 10.06.2025

Accepted: 12.06.2025

Published: 13.06.2025



Copyright: @ 2025 by the authors. Licensee Technobius, LLP, Astana, Republic of Kazakhstan. This article is an open access article distributed under the terms and conditions of the Creative Commons Attribution (CC BY-NC 4.0) license (<https://creativecommons.org/licenses/by-nc/4.0/>).



Effect of paraffine wax on the mobility of injection cement mortars

Zhibek Zhantlessova^{1,2,*}, Rauan Lukpanov^{1,2}, Duman Dyusseminov¹,
 Serik Yenkebayev^{1,2}, Denis Tsygulyov¹, Murat Karacasu³

¹L.N. Gumilyov Eurasian National University, Astana, Kazakhstan

²Solid Research Group, LLP, Astana, Kazakhstan

³Eskisehir Technical University, Eskisehir, Turkey

*Correspondence: proyekt.2022@bk.ru

Abstract. This study investigates the mobility of injection mortar and the influence of a paraffin-based modified additive on its flowability. The research pursues two main objectives: to develop the optimal composition of the additive and to evaluate its effect on mortar mobility at various concentrations. The additive significantly enhances mortar mobility, achieving peak performance at a 0.6% concentration. Further increases beyond 0.6% slightly reduce mobility but maintain an overall positive effect. Additionally, higher concentrations contribute to improved solution stability, as reflected by a reduced coefficient of variation. The additive not only improves the flow characteristics of injection mortar but also ensures its homogeneity and stability. The optimal additive dosage is determined to be within the range of 0.6% to 1.0% by cement weight. The application of digital image analysis in the study demonstrated high measurement accuracy and reproducibility, confirming its suitability for evaluating construction mixtures. The proposed additive shows strong potential for use in construction applications requiring high mortar mobility without compromising structural integrity.

Keywords: modified additive, soil stabilization, cement-sand, paraffin, mechanical properties.

1. Introduction

Injection mortars play a key role in construction and repair works, providing high strength to structures, preventing leaks, and increasing the durability of construction projects [1]. In modern construction, special attention is paid to improving the composition of construction materials to achieve optimal performance characteristics [2]. One of the urgent tasks is to increase the mobility of injection mortars, as it directly affects the quality of casting of structures, their strength, and durability [3]. However, an increase in the mobility of the mixture is often associated with an increase in the water-cement ratio [4], which leads to stratification of the mortar due to removal of active ions by excess water [5], loss of homogeneity [6], and deterioration of strength characteristics [7].

Modern methods of modification of injection mortars include using various chemical additives that change the properties of the mixture [8]. At the same time, there is a demand for additives that not only increase mobility but also provide stability and homogeneity of the mortar [9]. In this regard, using additives based on paraffin components is a promising direction. Such additives have many unique properties, including improving the flowability of the mixture and reducing the probability of its delamination [10], which makes them particularly relevant for use in harsh climatic conditions and with limited resources [11].

A pressing global imperative in the realm of modern construction materials science is to enhance the mobility of injected cement mortars without compromising their strength, homogeneity, and stability. This is of particular significance when working in areas that are difficult to access or in conditions of abrupt climatic changes, where the control of the water-cement ratio at the pouring site

is limited or impossible. In conventional methodologies, enhancing mobility is often pursued by increasing the B/C ratio. This approach is frequently accompanied by delamination, washout of active ions, reduction in strength, and diminished water resistance of the mortar.

To address this challenge, a concerted effort has been made in recent years to identify effective modifying additives. A particular focus has been placed on hydrophobizing compounds, with paraffin emulsions (PE) exhibiting particularly promising results. [12] found that PE can form water-repellent films in the capillaries of cement stone, reducing capillary water permeability and increasing corrosion resistance. However, when stearic acid is utilized as an emulsifier within an alkaline cement environment, a series of undesirable outcomes emerge, including dispersion destabilization, coalescence of paraffin globules, an augmentation in porosity, and a deterioration in strength properties.

The subsequent evolution of this approach is elucidated in the studies of [13], who proposed a method for the stabilization of paraffin emulsions through the utilization of acrylic and polycarboxylate plasticizers. These modified paraffin dispersions (MPD) exhibited stability within an alkaline environment, uniform distribution of paraffin within the cement stone structure in the form of mosaic films, and increased frost and water resistance.

The most advanced approach to the problem is posited in the works of [14], in which the utilization of complex additives (CA), including PE, non-ionogenic emulsifiers, and curing gas pedals (urea, calcium nitrate, sodium sulfate) is contemplated. The compositions in question have been demonstrated to produce a synergistic effect, characterized by an increase in cement stone density, an acceleration in strength gain, and an enhancement in resistance to water and salts. The use of urea- and sulfate-containing components yielded particularly favorable results.

Consequently, an analysis of contemporary research, encompassing publications in international journals (MDPI, ScienceDirect, Springer), enables the following conclusions to be drawn:

- Paraffin additives have been shown to promote the formation of hydrophobic films within the cement stone structure.
- Modified paraffin dispersions have demonstrated stability within alkaline environments.
- The incorporation of complex additives with paraffin has been demonstrated to enhance the resistance of cement materials to frost and salt attack.

Nevertheless, a number of significant issues remain to be adequately studied. A paucity of studies exists that systematically analyze the effect of paraffin additives on the mobility and stability of injection solutions at reduced W/C. Secondly, the influence of different dosages on the uniformity of paraffin distribution and homogeneity of the solution is evaluated fragmentarily. Thirdly, the extant works did not employ contemporary methodologies for digital image processing in the context of objective mobility assessment, a factor that has the potential to enhance the accuracy and reproducibility of measurements.

The objective of the present study is to develop a paraffin-modifying additive based on paraffin-cement suspension and to conduct a comprehensive study of its effect on the mobility, stability, and homogeneity of injected cement mortars at different water-cement ratios. The study will utilize digital imaging to analyze the results.

2. Methods

Table 1 below shows the content of the paraffin-based modifying additive (i.e., paraffin-cement suspension, hereinafter – PCS) and the reference mortar (cement-sand) used to mix the modified injection mortar compositions.

Table 1 – Composition of PCS and reference mortar

Component	Content, kg	
	PCS	Reference mortar
Portland cement [15]	1.0	0.5

Paraffin wax [16]	0.2	-
Sulfuric acid [17]	0.1	-
Tape water	1.0	0.3
Sand [18]	-	1.5

The composition of PCS included cement, paraffin wax, sulfuric acid (as a neutralizer), and water. The primary active component was paraffin wax, which was dissolved in the cement mixture to enhance the mobility and stability of the injection mortar. The sulfuric acid was necessary to facilitate the dispersion of hydrophobic paraffin in the aqueous medium via an exothermic neutralization reaction. The composition of reference mortar included cement, sand, and water.

Table 2 below shows the compositions of the injection mortar prepared for the study.

Table 2 – Studied compositions of injection mortar

No.	Content, kg			PCS, % by weight of reference mortar
	Water	Portland cement	Sand	
1*	0.15	0.5	1.5	-
2	0.15	0.5	1.5	0.2
3	0.15	0.5	1.5	0.4
4	0.15	0.5	1.5	0.6
5	0.15	0.5	1.5	0.8
6	0.15	0.5	1.5	1.0

*Reference composition of injection mortar

PCS was added to the reference mortar in varying concentrations from 0.2 to 1.0 % by weight of reference mortar (i.e., 2.15 kg). A total of 6 compositions were prepared, with three samples for each composition (to take an average). Then the water-cement ratio (W/C) of the compositions was modified from 0.3 to 0.6 by adding water in increments of 0.05 kg to each subsequent series.

Mobility testing was carried out for each series by the slump flow test according to [19] with some differences. Thus, to improve measurement precision, a digital image analysis was applied so that the photographs of each sample's spread were taken from a fixed height and angle, and processed in AutoCAD software to determine the spread area in cm² (Figure 1).

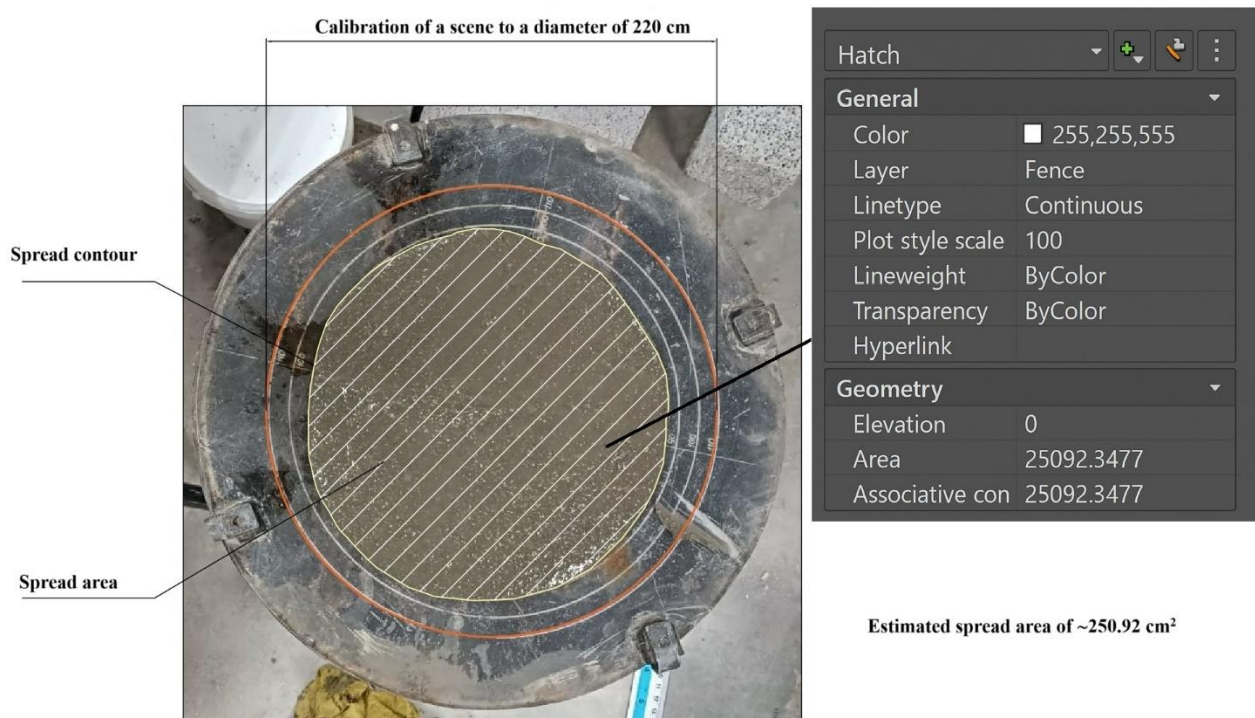


Figure 1 – Slump flow testing procedure

Tests on the viscosity of the injection solution were carried out following the modified method outlined in [19], entitled "Cements." The objective of this study is to determine the most effective methods for determining mobility. The primary approach involves the use of digital image processing to enhance the precision of measurements. The [20] method was utilized as an international analog.

The test equipment included the following: The standard Abrams cone is characterized by specific dimensions: its height is 300 millimeters, its base diameter is 200 millimeters, and its top base diameter is 100 millimeters.

The digital camera was mounted at a fixed height. The software known as AutoCAD has been utilized for the purpose of conducting spreading analysis.

Test Procedure: The mixture was subsequently poured into a cone without undergoing compaction. The cone was elevated in a vertical direction, thereby enabling the mortar to flow unimpeded on a horizontal surface. A photograph was obtained from an elevated vantage point, subsequently digitized in AutoCAD to ascertain the spreading area (in cm^2). The mortar samples were measured on three separate occasions, and the mean of these measurements was calculated. The experimental tests were conducted at water-cement ratios ranging from 0.3 to 0.6 and at additive concentrations ranging from 0.2% to 1.0% by weight of the control formulation.

The strength of modified mortars was evaluated by means of a compression method following [21] (or alternatively, [22]). The international analog is the method [23].

Test equipment: The apparatus under consideration is a hydraulic press with a maximum capacity of 2000 kN. The dimensions of the metal mold are 70.7 millimeters in length, width, and height, with each dimension measuring 70.7 millimeters. The vibration table is utilized for the purpose of compacting the specimens during the molding process. The following test procedure was employed: Control cubes were fabricated from each composition. The specimens were maintained under standard conditions (temperature 20 ± 2 °C, humidity not less than 90%) for a period of 28 days. The experimental tests were conducted using a press machine, with the load applied uniformly until the specimen fractured [23].

3. Results and Discussion

Figure 2 below shows the results of the slump flow tests of the sample.

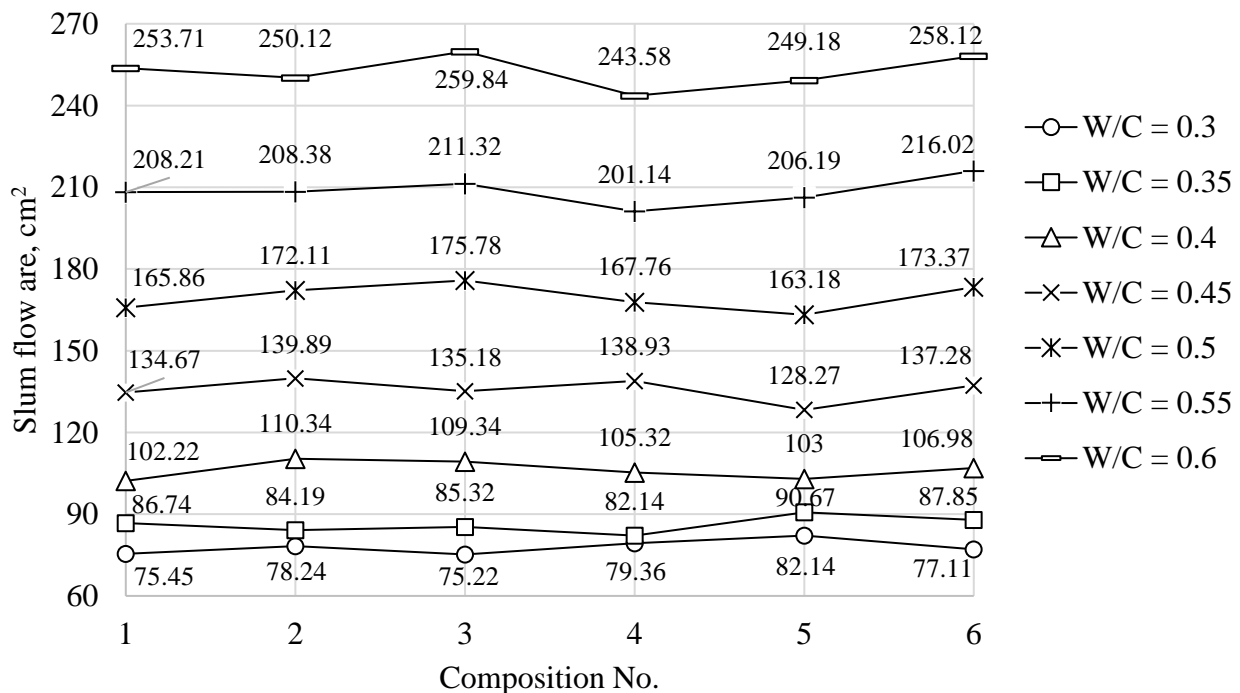


Figure 2 – Slump flow test results

Figure 2 shows the results of injection mortar slump tests as a function of the amount of Paraffin Cement Suspension (PCS) added. It can be seen that as the PCS content increases from 0.2% to 0.6%, there is a sharp increase in the spread area, indicating an improvement in the flowability of the mixture. As the PCS content is further increased up to 0.8-1.0%, the increase in flowability slows down, and at 1.0%, a slight decrease is observed, which may be due to excessive paraffin content increasing the viscosity of the system.

The main trend: the fluidity of the solution increases with the addition of PCS up to the optimum point (0.6%), after which a plateau or slight deterioration of the index is observed. This indicates that there is a critical level of additive above which the performance stabilizes or decreases.

Figure 3 below presents the sum of slump flow values, visually demonstrating the level of mobility stability of the compositions.

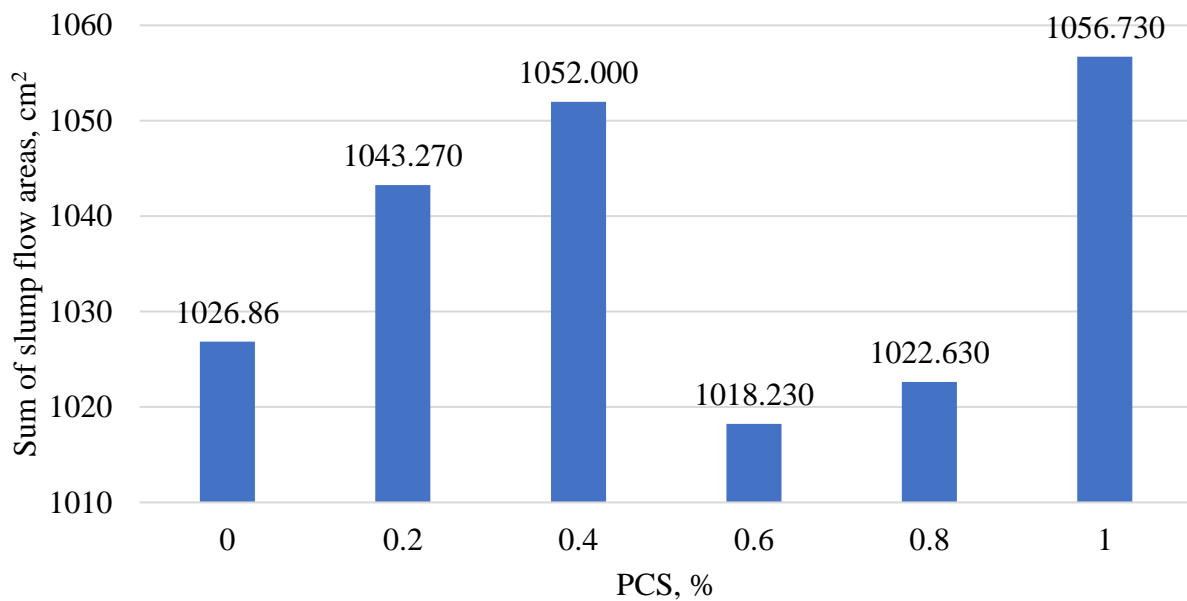


Figure 3 – Mortar mobility stability matrix

Figure 3 shows the mortar mobility stability matrix for different PCS contents and variation of the water-cement ratio. The maximum value of the total spreading area (1057 cm²) is achieved at a PCS content of 1.0%, indicating the highest mobility stability at this concentration. This confirms that higher PCS content helps to reduce the sensitivity of the formulation to changes in water-cement ratio.

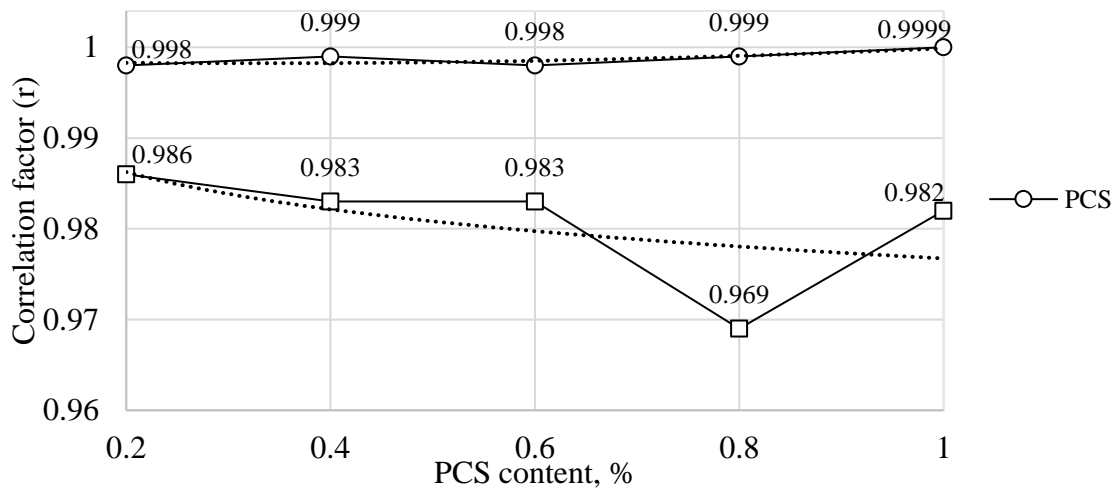


Figure 4 – Correlation analysis

Figure 4 illustrates the correlation between PCS content and the water-cement ratio. A strong positive correlation has been demonstrated between increasing PCS dosage and enhancing mortar flow stability. This phenomenon is attributed to the hydrophobic effect of paraffin, which mitigates the impact of excess water on the dispersed structure of the mortar.

The findings of the present study demonstrate a strong correlation with the results obtained in the study of [12], [13], [14], which demonstrated that modified paraffin emulsions promote the formation of hydrophobic films in the pores of cement stone, thereby increasing its stability and reducing capillary water permeability. In the work of [9], it was also noted that the incorporation of paraffin additives into mortar enhances its resistance to shrinkage deformations. This improvement is directly related to enhanced flowability and distribution uniformity.

[3] and [4] emphasize in their studies that an increase in flowability is possible at higher water-cement ratios. However, this increase is accompanied by a deterioration in strength properties. In contrast, the utilization of PCS in our study attained high flowability at low W/C, a critical aspect for injection mortars in hard-to-reach areas.

4. Conclusions

1) The modified paraffin-based additive presented in the study enhances the mobility of the injection mortar without increasing the water-cement ratio. This results in the maintenance of homogeneity and an increase in the stability of the composition.

2) The extant research has demonstrated that the additive, composed of paraffin-cement suspension (PCS), exerts a favorable influence on the flowability of injected cement mortar. The optimal effect is attained at the PCS dosage of 0.6% of the mass of the control mortar, at which the maximum spreading area and high mobility stability are observed.

3) Increasing the PCS concentration to 1.0% enhances mobility stability with changing water-cement ratios, rendering this additive particularly effective in variable humidity and temperature conditions.

4) The employment of digital image analysis in AutoCAD to estimate the spreading area of the mortar enhanced the precision of the measurements and the reproducibility of the results, thereby substantiating the method's applicability in laboratory settings.

5) A comparison with existing studies confirmed that the modified paraffin emulsions form hydrophobic films that reduce water absorption and increase the durability of cement stone without reducing the strength characteristics.

6) The developed paraffin-based additive is recommended for use in injection works, particularly in hard-to-reach and climatically unstable areas where high mobility and homogeneity are essential without increasing the water-cement ratio.

Acknowledgements

This research was funded by the Science Committee of the Ministry of Science and Higher Education of the Republic of Kazakhstan (Grant No. AP19680068).

References

- [1] H. Manalu and A. S. Wismogroho, "Development of Mortar for Repair of Cracked Concrete with Injection Method," *Journal of Technomaterial Physics*, vol. 4, no. 1, pp. 46–53, Feb. 2022, doi: 10.32734/jotp.v4i1.7779.
- [2] M. Butakova and S. Gorbunov, "Improving Performance Characteristics of Construction Materials Manufactured by Pressing Technology," *Procedia Eng*, vol. 206, pp. 814–818, 2017, doi: 10.1016/j.proeng.2017.10.556.
- [3] V. Pesaralanka and V. C. Khed, "Flowability and compressive strength test on self compacting mortar using graphene oxide," *Mater Today Proc*, vol. 33, no. 4, pp. 491–495, Aug. 2020, doi: 10.1016/j.matpr.2020.05.067.
- [4] V. G. Haach, G. Vasconcelos, and P. B. Lourenço, "Influence of aggregates grading and water/cement ratio in workability and hardened properties of mortars," *Constr Build Mater*, vol. 25, no. 6, pp. 2980–2987, Jun. 2011, doi: 10.1016/j.conbuildmat.2010.11.011.
- [5] S. Gupta and H. W. Kua, "Effect of water entrainment by pre-soaked biochar particles on strength and permeability of cement mortar," *Constr Build Mater*, vol. 159, pp. 107–125, Jan. 2018, doi: 10.1016/j.conbuildmat.2017.10.095.

- [6] S. B. Singh, P. Munjal, and N. Thammishetti, "Role of water/cement ratio on strength development of cement mortar," *Journal of Building Engineering*, vol. 4, pp. 94–100, Dec. 2015, doi: 10.1016/j.jobbe.2015.09.003.
- [7] S. A. Ayanlere, S. O. Ajamu, S. O. Odeyemi, O. E. Ajayi, and M. A. Kareem, "Effects of water-cement ratio on bond strength of concrete," *Mater Today Proc*, vol. 86, pp. 134–139, 2023, doi: 10.1016/j.matpr.2023.04.686.
- [8] W. Du *et al.*, "Effect of temperatures on self-healing capabilities of concrete with different shell composition microcapsules containing toluene-di-isocyanate," *Constr Build Mater*, vol. 247, p. 118575, Jun. 2020, doi: 10.1016/j.conbuildmat.2020.118575.
- [9] M. Wyrzykowski, S. Ghourchian, B. Münch, M. Griffo, A. Kaestner, and P. Lura, "Plastic shrinkage of mortars cured with a paraffin-based compound – Bimodal neutron/X-ray tomography study," *Cem Concr Res*, vol. 140, p. 106289, Feb. 2021, doi: 10.1016/j.cemconres.2020.106289.
- [10] R. A. Razak *et al.*, "Paraffin as a Phase Change Material in Concrete for Enhancing Thermal Energy Storage," *IOP Conf Ser Mater Sci Eng*, vol. 743, no. 1, p. 012012, Feb. 2020, doi: 10.1088/1757-899X/743/1/012012.
- [11] V. Zetola, L. J. Claros-Marfil, A. G. Santos, and Fco. J. N. González, "Effect of Paraffin and Silica Matrix Phase Change Materials on Properties of Portland Cement Mortars," *Materials*, vol. 14, no. 4, p. 921, Feb. 2021, doi: 10.3390/ma14040921.
- [12] S. Glavina, *Cement mortars and concretes with additives of modified paraffin dispersions*. Moscow: Mendelev University of Chemical Technology of Russia, 2012.
- [13] N. H. Belous *et al.*, "The effect of composite paraffine-containing additives on properties of small-grain Portland cement concretes," *Proceedings of the National Academy of Sciences of Belarus, Chemical Series (Vesci Nacyanal'naj akademii navuk Belarusi. Serya himichnyh navuk)*, no. 4, pp. 93–98, 2014, doi: 10.29235/1561-8331-2021-57-1-94-100.
- [14] N. H. Belous, S. P. Rodtsevich, O. N. Opanasenko, and N. P. Krutko, "Influence of modifying additives on the structural characteristics and properties of Portland cement concretes," *Proceedings of the National Academy of Sciences of Belarus, Chemical Series*, vol. 57, no. 1, pp. 94–100, Feb. 2021, doi: 10.29235/1561-8331-2021-57-1-94-100.
- [15] Stroydk, "Cement Semey M450, M500." Accessed: Jun. 01, 2025. [Online]. Available: <https://stroydk.kz/tovary/smesi/tsement/tsement-m-450-semeycement>
- [16] Snabtechmet, "Sulphuric acid H2SO4." Accessed: Jun. 01, 2025. [Online]. Available: https://snabtechmet.kz/product/sernaja_kislota_h2so4_1_litr/
- [17] SNGgroupKZ, "Technical paraffin." Accessed: Jun. 01, 2025. [Online]. Available: <https://snggroup.kz/product/parafin-tehnicheskij>
- [18] Snabservice, "Construction sand medium by GOST 8736-2014." Accessed: Jun. 01, 2025. [Online]. Available: <https://snabservice.kz/product/pesok-stroitelnyj-srednij-30-kg-gost-8736-2014/>
- [19] "GOST 310.4-81 Cements. Methods for determination of bending and compressive strengths," 2003.
- [20] ASTM, *ASTM C143/C143M-15, Standard Test Method for Slump of Hydraulic-Cement Concrete*. West Conshohocken, PA: ASTM International, 2015.
- [21] *GOST 30744-2001. Cements. Methods of testing with using polyfraction standard sand*. 2021, p. 36.
- [22] *GOST 310.2-76 Cements. Test methods*. 1976.
- [23] ASTM, *ASTM C109/C109M Standard Test Method for Compressive Strength of Hydraulic Cement Mortars (Using 2-in. or [50-mm] Cube Specimens)*. West Conshohocken, PA: ASTM International, 2020.

Information about authors:

Zhibek Zhantlesova – 1) PhD Student, L.N. Gumilyov Eurasian National University, Astana, Kazakhstan; 2) Junior Researcher, Solid Research Group, LLP, Astana, Kazakhstan, zhibek81@mail.ru

Rauan Lukpanov – 1) PhD, Professor, L.N. Gumilyov Eurasian National University, Astana, Kazakhstan; 2) Scientific Supervisor, Solid Research Group, LLP, Astana, Kazakhstan, rauan_82@mail.ru

Duman Dyusseminov – Candidate of Technical Sciences, Associate Professor, L.N. Gumilyov Eurasian National University, Astana, Kazakhstan, duseminov@mail.ru

Serik Yenkebayev – 1) PhD, Associate Professor, L.N. Gumilyov Eurasian National University, Astana, Kazakhstan; 2) Senior Researcher, Solid Research Group, LLP, Astana, Kazakhstan, yenkebayev-serik@mail.ru

Denis Tsygulyov – Candidate of Technical Sciences, Associate Professor, L.N. Gumilyov Eurasian National University, Astana, Kazakhstan, denis_72@mail.ru

Murat Karacasu – PhD, Professor, Eskisehir Technical University, Eskisehir, Turkey, muratk@ogu.edu.tr

Author Contributions:

Zhibek Zhantlesova –methodology, resources, data collection, testing, modeling, analysis.

Rauan Lukpanov – concept, methodology, analysis

Duman Dyusseminov – analysis, interpretation, drafting.

Serik Yenkebayev – resources, funding acquisition.

Denis Tsygulyov – data collection, visualization, testing.

Murat Karacasu – editing.

Conflict of Interest: The authors declare no conflict of interest.

Use of Artificial Intelligence (AI): The authors declare that AI was not used.

Received: 03.02.2025

Revised: 12.06.2025

Accepted: 15.06.2025

Published: 17.06.2025



Copyright: @ 2025 by the authors. Licensee Technobius, LLP, Astana, Republic of Kazakhstan. This article is an open access article distributed under the terms and conditions of the Creative Commons Attribution (CC BY-NC 4.0) license (<https://creativecommons.org/licenses/by-nc/4.0/>).



Investigation of the properties of fly ash and slag-based geopolymer concrete containing waste glass aggregates

Zhuzimkul Urkinbayeva¹, Assel Jexembayeva², Marat Konkanov³, Samal Akimbekova^{1,*},
 Lailya Zhaksylykova⁴, Tariq Umar⁵

¹Department of Technology of Industrial and Civil Engineering, L.N. Gumilyov Eurasian National University, Astana, Kazakhstan

²Department of Innovative Development, L.N. Gumilyov Eurasian National University, Astana, Kazakhstan

³Department of Innovative Development, L.N. Gumilyov Eurasian National University, Astana, Kazakhstan

⁴Department of Architecture, L.N. Gumilyov Eurasian National University, Astana, Kazakhstan

⁵School of Architecture and Environment, University of the West of England, Bristol, United Kingdom

*Correspondence: sammi_ok@mail.ru

Abstract. This paper evaluates the geopolymer concrete produced using industrial waste and waste glass obtained by crushing glass materials. Geopolymer concrete mixtures were prepared with a water-to-binder ratio of 0.35 and an alkali activator solution to binder ratio (AAS/B) of 0.5 and 0.4. The partial substitution of sand by waste glass was 10%, 20% and 30%. Laboratory results showed that the compressive strength of geopolymer concrete increased with the addition of waste glass for a geopolymer concrete with AAS/B = 0.5, but decreased for AAS/B = 0.4. The expansion due to the alkali-silica reaction (ASR) was below 0.1% which is the expansion limit. The shrinkage of geopolymer concrete during drying decreases with an increase in glass content. The results of this study indicate that using glass as a partial sand substitute in geopolymer concrete provides sufficient mechanical properties. In addition, the production of this concrete will improve environmental conditions by reducing the extraction of raw materials and recycling waste glass.

Keywords: geopolymer concrete, industrial waste, waste glass aggregate, alkali-silica reaction, alkali activator solution.

1. Introduction

Geopolymer concrete is an alternative construction material to traditional Portland cement concrete, made by activation of aluminosilicate materials such as fly ash, slag, silica fume, and metakaolin using the alkaline solution [1]. Geopolymerization is a reaction process among aluminosilicate materials and alkali metal silicates, resulting in the formation of a strong polymer [2]. The final state performance of the geopolymer concrete depends on the type of constituents used in the mixture, including binder material, activators, aggregates, and required admixtures. The tectoluminosilicate type of three-dimensional structure in the geopolymer grid provides nanoporous characteristics, allowing chemically and physically bound water molecules (hydroxyl groups – OH) to evaporate when heated [3]. This property prevents the boiling of water and the destruction of concrete from the inside, as happens with Portland cement. In this regard, the strength of the geopolymer concrete obtained from the experiment will be comparable to that of traditional cement-based concrete. The main advantages of geopolymer concrete are lower CO₂ emissions, fire and corrosion resistance, reduction of raw materials usage, recycled industrial waste, and cost savings [4].

The continuously increasing demands for enhancing environmental sustainability and energy efficiency in the construction materials industry, along with the growing emphasis on waste utilization, drive intensive research in the development of binding materials that incorporate waste

from the fuel industry [5]. Construction activities are the most materials-intensive human endeavors. Each year, billions of tons of mineral raw materials are extracted from the natural environment to produce traditional cement-based concrete and other building materials. Global cement production is approximately 3.5 billion tons per year [6]. Moreover, cement production is one of the issues of global carbon dioxide (CO₂) emissions, taking a part of approximately 7% [7]. Therefore, it is extremely important to partially replace traditional concrete production with geopolymer concrete, which utilizes industrial waste in order to reduce raw materials extraction and CO₂ emission [8]. However, the application of industrial waste might negatively affect the performance of the concrete. For example, the excessive use of fly ash, slag, and silica fume might reduce the strength of the geopolymer concrete due to the segregation compared to the Portland cement concrete [9]. Another global concern is that large quantities of glass are discarded in landfills each year. In addition, sand remains the primary natural resource for concrete production. To address this issue, waste glass can serve as a substitute for sand, thereby reducing global sand consumption [10].

Geopolymer concrete has lower workability compared to the Portland cement-based concrete [11]. Moreover, the increase of slag compared to fly ash decreases the workability. However, it was investigated that the inclusion of slag helps to increase the strength of geopolymer concrete, making it reasonable to use the combination of fly ash and slag to produce geopolymer concrete. Furthermore, it was found that the application of NaOH solution with a molarity of 10M is better than 8M for durability of geopolymer concrete [12]. The source of fly ash also has an impact on the compressive strength due to the different particle size distribution and microstructure [13]. Usage of glass in concrete production leads to material cracking due to the expansion caused by alkali-silica reaction (ASR) [14]. In this case, the utilization of fly ash and slag can reduce the potential expansion.

There are many studies focused on fresh properties and compressive strength of geopolymer concrete, but few research works were done on the alkali-silica reactivity of geopolymer concrete containing waste glass aggregate. Therefore, there is a need to investigate and find optimal geopolymer concrete mixtures containing glass materials.

Since glass has similar characteristics to sand, such as chemical composition and physical properties, it can be hypothesized that waste glass can be incorporated as a partial sand replacement material in the production of geopolymer concrete [15].

The goal of this article is to use industrial byproducts and glass waste to identify the optimal mixture proportions to produce geopolymer concrete with acceptable strength and durability performances that can be used in the construction industry.

2. Methods

Seven different mixture compositions were prepared to determine the effect of two variables, such as glass and alkaline activator solution content, on the performance of concrete based on the previous studies [16]. The proportions of each material are presented in Table 1. A binder material consisting of 60% fly ash and 40% slag was used, with partial replacement of sand by glass waste in the proportions of 0%, 10%, 20%, and 30%. For all mixtures, the water-to-binder ratio was set at 0.15. However, the ratio of the alkaline activator solution to the binder (AAS/B) varied between the two groups to analyze the effect of the alkaline activator solution concentration on the properties of geopolymer concrete [17]. For the first four mixtures, the AAS/B value was set at 0.5, while for the remaining three mixtures, it was set at 0.4. The molarity of NaOH for all 8 mixtures was 10M. Sodium silicate (Na₂SiO₃) and sodium hydroxide (NaOH) were used as alkaline activators since application of these solutions results in the formation of a strong bond between binder and aggregates [18].

Table 1 – Proportions of Geopolymer mortar mixtures, kg/m³

Mixtures	Fly ash	Slag	Sand	Glass	Na ₂ SiO ₃	NaOH	Plast	Water
GPC 0.5-0	556.7	371.1	397.6	-	309.0	44.2	12.1	95.42
GPC 0.5-10	556.7	371.1	357.8	39.8	309.0	44.2	12.1	95.42

GPC 0.5-20	556.7	371.1	318.1	79.5	309.0	44.2	12.1	95.42
GPC 0.5-30	556.7	371.1	278.3	119.3	309.0	44.2	12.1	95.42
GPC 0.4-10	569.2	379.4	365.9	40.7	253.0	36.1	12.1	146.3
GPC 0.4-20	569.2	379.4	325.3	81.3	253.0	36.1	12.1	146.3
GPC 0.4-30	569.2	379.4	284.6	122.0	253.0	36.1	12.1	146.3

Note: 0.5 and 0.4 are the content of AAS/B; 0, 10, 20, and 30 are the fraction of glass in %.

Energy Dispersive Spectral (EDS) analysis was conducted using the 5EDX9000V spectrometer, model 200-ES1202344536, 220V 50/60Hz, to determine the chemical composition of fly ash, slag, sand, and glass [19]. This test is required to analyze the distribution of chemical compounds and define the validity of using industrial by-products and waste glass as aggregates to produce geopolymer concrete. The results of the chemical composition analysis test are presented in Table 2. The main components of the glass material are silica oxide (71.86 %), sodium oxide (10.84 %), and calcium oxide (12.96 %) [20]. Since the major portion of chemical compounds in glass is silica, as well as in sand, the results justify the application of glass as a partial sand substitution material.

Table 2 – Chemical Composition of Fly ash, Slag, Sand, and Glass [%]

Waste	SiO ₂	Al ₂ O ₃	Fe ₂ O ₃	CaO	SO ₃	MgO	TiO ₂	Na ₂ O	K ₂ O	MnO
Fly ash	60.55	28.12	6.74	5.59	0.04	0.65	1.05	0.42	0.19	0.09
Slag	61.46	28.34	5.37	5.62	0.04	1.69	1.29	0.48	1.17	0.09
Sand	49.79	14.33	6.52	13.60	0.56	0.75	0.84	4.53	3.16	0.28
Glass	71.86	2.530	0.64	12.96	0.04	0.55	0.12	10.84	0.31	0.04

Fly ash is the non-combustible residue that forms from the mineral impurities in fuel during its complete combustion. The chemical composition of fly ash is primarily represented by four elements: aluminium (Al), silicon (Si), calcium (Ca), and, in smaller amounts, iron (Fe). River sand is a type of rock formed by the erosion of hard minerals. Its chemical formula is SiO₂, or silicon dioxide [21]. Depending on the chemical composition of the slag melts, the rapidly cooled slags develop an amorphous structure. This prevents the formation of a crystalline structure and makes the slag a reactive material with better bonding properties. The chemical composition of blast furnace slags is primarily represented by four oxides: CaO, MgO, Al₂O₃, and SiO₂, with iron oxides present in small quantities.

Sand and waste glass were sieved to determine the size distribution and use the particular amount of each size during the mixing process of geopolymer concrete.

The process of preparing samples and conducting tests began with the preparation of the alkaline activator solution 24 hours before mixing the geopolymer concrete [22]. On the mixing day, all materials were combined using a laboratory mixer. Initially, the binder materials were mixed for 60 seconds, followed by the addition of the alkaline activator solution, which was mixed for 120 seconds. The mixture was then stirred for another 240 seconds while incorporating fillers. A 90-second pause was taken to scrape off any material adhering to the walls of the mixing bowl. Finally, all components were mixed again for an additional 150 seconds. Once the mixing process was complete, the fresh homogeneous mixture was poured into molds of different sizes, depending on the specific tests. After 24 hours, the samples were demolded and left to air dry at room temperature and about 45% of relative humidity until the testing day.

Compressive strength, ASR, and drying shrinkage tests were done to determine the mechanical and durability properties of the geopolymer concrete samples. All of these tests were done according to the standards of the American Society for Testing and Materials (ASTM).

The compressive strength test was done based on [23]. For this test, 50 mm cube samples were cast and cured at room temperature. These samples were tested using the universal testing machine on the 7th, 14th, and 28th day [24].

The ASR test was done following [25]. Four bar samples, each measuring 25×25×285 mm, were prepared for each mixture and left air cured at room temperature for one day. After curing, the samples were immersed in water-filled containers, which were then placed in an oven at 80 ± 2 °C for 24 hours. Subsequently, the initial length of all samples was recorded as the 0-day measurement. The samples were then transferred to a container containing a 1M NaOH solution and again stored at 80 ± 2 °C to investigate the effect of a harsh environment on the length change and potential cracking [26]. Measurements were taken at 3- and 4-day intervals up to the 28th day to assess the relative expansion of geopolymer concrete.

The drying shrinkage test was done based on [27]. For each mixture, bar samples with a size 25×25×285 mm were cast and cured at room temperature and relative humidity approximately equal to 45% [28]. Every 3- and 4-day interval for 3 months, the length change and weight loss of each sample were measured to analyze the moisture loss and the effect of glass particles on the performance of geopolymer concrete.

3. Results and Discussion

The results of compressive strength tests for each geopolymer mixture aged 7, 14, and 28 days are demonstrated in Figure 1.

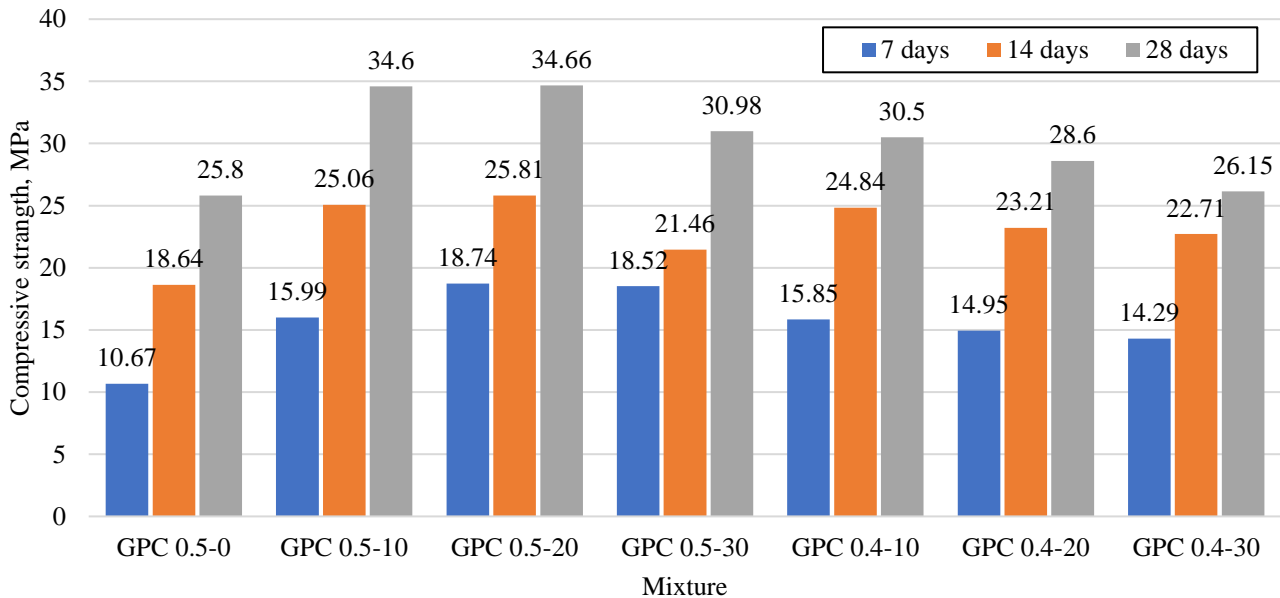


Figure 1 – Compressive strength of geopolymer concrete

Based on Figure 1 above, the compressive strength of each geopolymer concrete increases after a certain period of time. With the ratio AAS/B = 0.50, the mixtures containing waste glass demonstrated higher compressive strength compared to the control mixture with a 0% glass content, which explains the improved gel mesh of the geopolymer system due to dissolved silica particles in an alkaline medium [29]. With the same AAS/B = 0.50 ratio, geopolymer mixtures containing 10 % and 20 % glass exhibited the same maximum strength of approximately 35 MPa after 28 days; however, both showed unequal compressive strengths at 7 and 14 days. Further increasing the glass content to 30 % slightly reduced the compressive strength of the geopolymer mixture to about 31 MPa, which may be attributed to poor bonding between the glass and the binder at high glass content due to the smooth surface of the glass. Therefore, even though the addition of glass increases the strength at lower glass content, the further increase of glass to approximately higher than 20% sand replacement has a negative effect on the performance of geopolymer concrete.

Additionally, the test results indicated a negative impact of reduced alkali-activated solution (AAS) content in the mixture on the strength development of geopolymer concrete. For instance, the

GPC0.4-10 mixture, containing 10% glass, exhibited lower compressive strength after 28 days compared to the GPC0.5-10 mixture with the same glass content (30.5 MPa vs. 34.6 MPa). In fact, the silica and alumina contained in fly ash and slags primarily contribute to an increase in the strength properties of the geopolymer mixture due to the reactivity of the components. The concentration of AAS affects reactivity. At lower AAS concentrations, silica and aluminum monomers are released to a lesser extent, and the aluminosilicate reaction occurs weakly, resulting in reduced geopolymerization due to poor gel formation, which is essential for strengthening and enhancing the material's strength [30]. Similarly, in the case of 0.5 AAS/B, increasing the glass content to 20 % and 30 % led to a decrease in strength to 28.6 MPa and 26.2 MPa, respectively.

Figure 2 shows the expansion behavior of geopolymer concrete mixtures subjected to ASR.

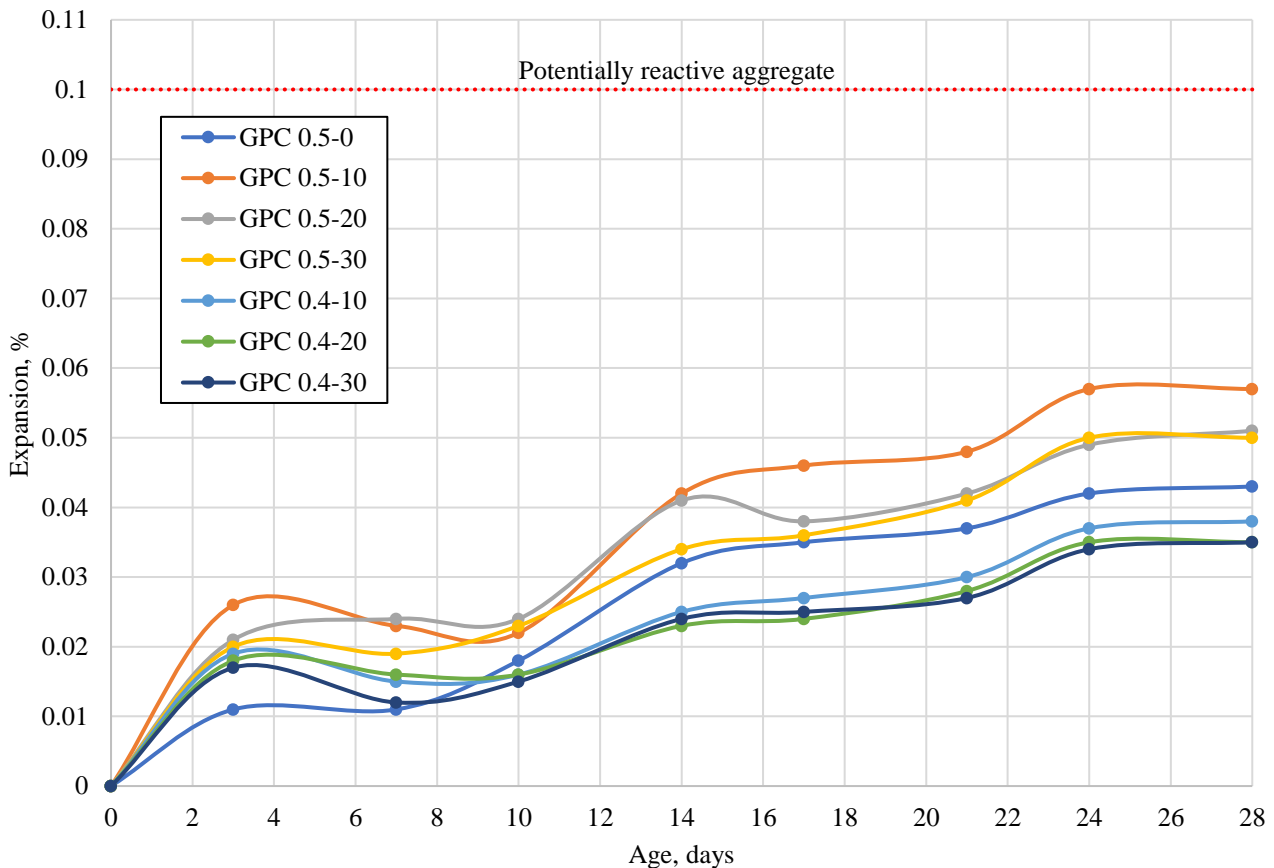


Figure 2 – ASR of geopolymer concrete

As shown in Figure 2 above, regardless of the AAS/B ratio and the WGS replacement percentage, all geopolymer concrete mixtures exhibit minimal expansion, significantly lower than the 0.1% threshold set by [31] for potentially reactive aggregates. These results align with investigations of [32], where the mechanisms responsible for mitigating ASR expansion in geopolymer concrete containing fly ash and slag are investigated. The amorphous components in fly ash and slag consume a substantial portion of the alkalis in the pore solution, transforming them into cementitious binders. This process reduces alkali concentration through dilution and fixes alkalis within the hydration reaction, thereby limiting the formation of ASR gel compared to ordinary Portland cement-based concrete.

Furthermore, increasing the waste glass content does not considerably increase the expansion due to the ASR. This may be attributed to the influence of fly ash and slag, which lower the alkali content in the binder and promote the formation of non-expansive lime-silica gel, as the silicate components in glass contribute to geopolymerization [32]. The ASR test results confirm that fly ash and slag-based geopolymer concrete effectively controls expansion in mixtures containing waste glass aggregates, as none exceeded the 0.1% expansion limit.

Figure 3 shows the drying shrinkage of the geopolymer mixtures.

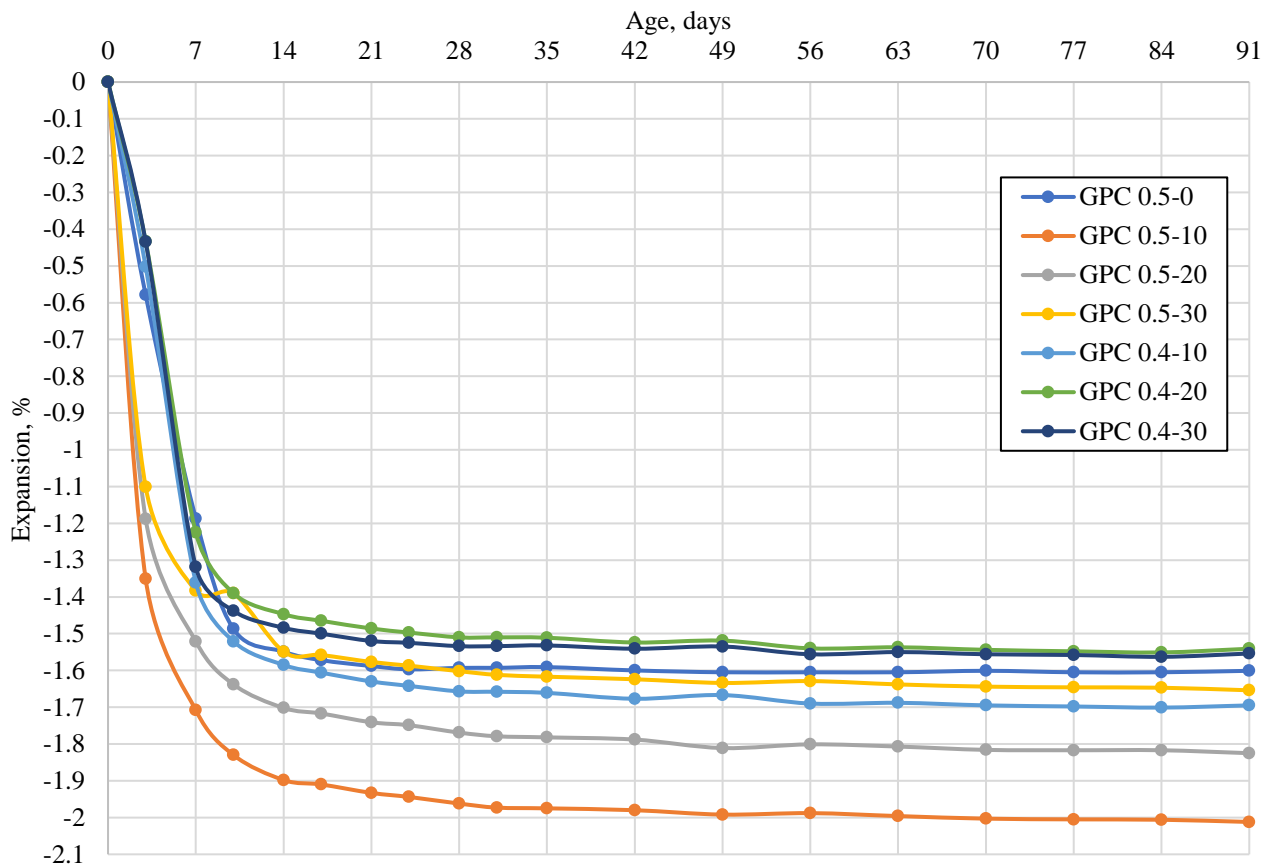


Figure 3 – Drying Shrinkage of geopolymer concrete

As shown in Figure 3 above, the GPC0.5-10 mixture experienced the highest shrinkage, with a length change of -2.03% by day 91. Increasing the glass content reduced the drying shrinkage of the geopolymer mixture, regardless of the different AAS/B values. The decrease in shrinkage during drying due to an increase in the filler content in the glass is explained by the reduced water absorption capacity of the glass. However, the geopolymer mixture containing 100 % sand had a lower shrinkage during drying compared to GPS 0.5-10.

Studies have confirmed that mixtures of geopolymers with AAS/B = 0.50 showed greater shrinkage during drying than those with AAS/B = 0.40. This is explained by the increased tensile stress in the capillary pores of the geopolymer mixture, which contributes to higher shrinkage during drying [33].

4. Conclusion

In this study, the chemical properties of cementitious materials and aggregates and the mechanical properties of geopolymer concrete produced by partially replacing sand with glass were obtained. When the ratio of the alkaline activator solution to binder is 0.50, the addition of glass enhances the compressive strength. However, at AAS/B = 0.40, the inclusion of glass reduces compressive strength. The application of fly ash and slag helps to maintain the expansion of geopolymer concrete with glass due to the ASR below 0.1%. Regardless of the alkaline activator to binder ratio, the gradual increase in glass content decreases the drying shrinkage of the geopolymer mixture.

Overall, the use of large quantities of local industrial and solid municipal waste, such as fly ash, blast furnace slag, and glass, will contribute to environmental protection. These materials can be used to produce geopolymer concrete with a cement-free binder that achieves a compressive strength

of 35 MPa without thermal treatment. Utilizing glass as a sand replacement material is reasonable, as geopolymer concrete containing glass exhibits adequate strength and durability properties. This geopolymer concrete can be used as a construction material for small buildings, statues, and paving with lower loads.

This study has some potential limitations. The limited number of mixture types and conducted tests does not show the full scale of durability properties of geopolymer concrete. Therefore, there is a need to conduct more laboratory work to evaluate and determine the full potential of geopolymer concrete with waste glass.

Acknowledgments

This research is funded by the Committee of Science of the Ministry of Science and Higher Education of the Republic of Kazakhstan (Grant No. BR21882278 «Establishment of a construction and technical engineering center to provide a full cycle of accredited services to the construction, road-building sector of the Republic of Kazakhstan»).

References

- [1] C.-K. Ma, A. Z. Awang, and W. Omar, "Structural and material performance of geopolymer concrete: A review," *Constr Build Mater*, vol. 186, pp. 90–102, Oct. 2018, doi: 10.1016/j.conbuildmat.2018.07.111.
- [2] S. Chowdhury, S. Mohapatra, A. Gaur, G. Dwivedi, and A. Soni, "Study of various properties of geopolymer concrete – A review," *Mater Today Proc*, vol. 46, pp. 5687–5695, 2021, doi: 10.1016/j.matpr.2020.09.835.
- [3] N. A. Eroshkina and A. A. Mishanov, "Vodostojkost geopolimernyh vyazhushih s kompleksnoj dobavkoj," in *Teoriya i praktika povysheniya effektivnosti stroitelnyh materialov: Sbornik nauchnyh trudov I Vserossijskoj konferencii studentov, aspirantov i molodyh uchenykh*, Penza: PGUAS, 2006, pp. 88–91.
- [4] A. Hassan, M. Arif, and M. Shariq, "Use of geopolymer concrete for a cleaner and sustainable environment – A review of mechanical properties and microstructure," *J Clean Prod*, vol. 223, pp. 704–728, Jun. 2019, doi: 10.1016/j.jclepro.2019.03.051.
- [5] T. Van Lam, N. Xuan Hung, V. Kim Dien, B. I. Bulgakov, S. I. Bazhenova, and O. V. Aleksandrova, "Geopolymer concrete made using large-tonnage technogenic waste," *Stroitel'stvo: nauka i obrazovanie [Construction: Science and Education]*, vol. 11, no. 2, pp. 17–37, Jun. 2021, doi: 10.22227/2305-5502.2021.2.2.
- [6] Heidelberg, "Itogi 2022 goda. Proizvodstvo cementa v Respublike Kazahstan," Heidelberg Materials. Accessed: Jun. 26, 2025. [Online]. Available: <https://www.cem.kz/ru/news/30-itogi-2022-goda-proizvodstvo-tsementa-v-respublike-kazahstan.html>
- [7] Md. N. N. Khan and P. K. Sarker, "Effect of waste glass fine aggregate on the strength, durability and high temperature resistance of alkali-activated fly ash and GGBFS blended mortar," *Constr Build Mater*, vol. 263, p. 120177, Dec. 2020, doi: 10.1016/j.conbuildmat.2020.120177.
- [8] Nesterov V.Yu., Kalashnikov V.I., Yu. S. Kuznecov, Yu. V. Gavrilova, and N. A. Eroshkina, "Silicitovye geopolimery: pervye shagi k sozdaniyu materiala budushhego," in *Aktualnye voprosy stroitelstva. Materialy MNTK*, Saransk, 2004, p. 160.
- [9] G. S. Ryu, Y. B. Lee, K. T. Koh, and Y. S. Chung, "The mechanical properties of fly ash-based geopolymer concrete with alkaline activators," *Constr Build Mater*, vol. 47, pp. 409–418, Oct. 2013, doi: 10.1016/j.conbuildmat.2013.05.069.
- [10] N. Almesfer and J. Ingham, "Effect of Waste Glass on the Properties of Concrete," *Journal of Materials in Civil Engineering*, vol. 26, no. 11, Nov. 2014, doi: 10.1061/(ASCE)MT.1943-5533.0001077.
- [11] R. R. Bellum, M. Al Khazaleh, R. K. Pilla, S. Choudhary, and C. Venkatesh, "Effect of slag on strength, durability and microstructural characteristics of fly ash-based geopolymer concrete," *Journal of Building Pathology and Rehabilitation*, vol. 7, no. 1, p. 25, Dec. 2022, doi: 10.1007/s41024-022-00163-4.
- [12] A. E. Kurtoğlu *et al.*, "Mechanical and durability properties of fly ash and slag based geopolymer concrete," *Advances in Concrete Construction*, vol. 6, no. 4, 2018, doi: 10.12989/acc.2018.6.4.345.
- [13] L. N. Assi, E. (Eddie) Deaver, M. K. ElBatanouny, and P. Ziehl, "Investigation of early compressive strength of fly ash-based geopolymer concrete," *Constr Build Mater*, vol. 112, pp. 807–815, Jun. 2016, doi: 10.1016/j.conbuildmat.2016.03.008.
- [14] Md. N. N. Khan and P. K. Sarker, "Alkali silica reaction of waste glass aggregate in alkali activated fly ash and GGBFS mortars," *Mater Struct*, vol. 52, no. 5, p. 93, Oct. 2019, doi: 10.1617/s11527-019-1392-3.
- [15] K. H. Tan and H. Du, "Use of waste glass as sand in mortar: Part I – Fresh, mechanical and durability properties," *Cem Concr Compos*, vol. 35, no. 1, pp. 109–117, Jan. 2013, doi: 10.1016/j.cemconcomp.2012.08.028.
- [16] P. Cong and Y. Cheng, "Advances in geopolymer materials: A comprehensive review," *Journal of Traffic and Transportation Engineering (English Edition)*, vol. 8, no. 3, pp. 283–314, Jun. 2021, doi: 10.1016/j.jtte.2021.03.004.

- [17] M. T. Ghafoor, Q. S. Khan, A. U. Qazi, M. N. Sheikh, and M. N. S. Hadi, "Influence of alkaline activators on the mechanical properties of fly ash based geopolymer concrete cured at ambient temperature," *Constr Build Mater*, vol. 273, p. 121752, Mar. 2021, doi: 10.1016/j.conbuildmat.2020.121752.
- [18] T. Phoo-ngernkham, A. Maegawa, N. Mishima, S. Hatanaka, and P. Chindaprasirt, "Effects of sodium hydroxide and sodium silicate solutions on compressive and shear bond strengths of FA-GBFS geopolymer," *Constr Build Mater*, vol. 91, pp. 1–8, Aug. 2015, doi: 10.1016/j.conbuildmat.2015.05.001.
- [19] A. Fauzi, M. F. Nuruddin, A. B. Malkawi, and M. M. A. B. Abdullah, "Study of Fly Ash Characterization as a Cementitious Material," *Procedia Eng*, vol. 148, pp. 487–493, 2016, doi: 10.1016/j.proeng.2016.06.535.
- [20] G. N. Dolzhenko, *TS 5870-006-30993911-2014 Geopolymer Concrete. Technical Conditions*. Chelyabinsk: Innovation Technopark Arkh & Stroy, 2014.
- [21] B. Meskhi *et al.*, "Analytical Review of Geopolymer Concrete: Retrospective and Current Issues," *Materials*, vol. 16, no. 10, p. 3792, May 2023, doi: 10.3390/ma16103792.
- [22] P. Pavithra, M. Srinivasula Reddy, P. Dinakar, B. Hanumantha Rao, B. K. Satpathy, and A. N. Mohanty, "A mix design procedure for geopolymer concrete with fly ash," *J Clean Prod*, vol. 133, pp. 117–125, Oct. 2016, doi: 10.1016/j.jclepro.2016.05.041.
- [23] ASTM, *ASTM C109/C109M Standard Test Method for Compressive Strength of Hydraulic Cement Mortars (Using 2-in. or [50-mm] Cube Specimens)*. West Conshohocken, PA: ASTM International, 2020.
- [24] M. Padmakar, B. Barhmaiah, and M. Leela Priyanka, "Characteristic compressive strength of a geo polymer concrete," *Mater Today Proc*, vol. 37, pp. 2219–2222, 2021, doi: 10.1016/j.matpr.2020.07.656.
- [25] "Test Method for Determining the Potential Alkali-Silica Reactivity of Combinations of Cementitious Materials and Aggregate (Accelerated Mortar-Bar Method)," Oct. 01, 2022, *ASTM International, West Conshohocken, PA*. doi: 10.1520/C1567-22.
- [26] J. Lei, J. Fu, and E.-H. Yang, "Alkali-Silica Reaction Resistance and Pore Solution Composition of Low-Calcium Fly Ash-Based Geopolymer Concrete," *Infrastructures (Basel)*, vol. 5, no. 11, p. 96, Nov. 2020, doi: 10.3390/infrastructures5110096.
- [27] "Test Method for Drying Shrinkage of Mortar Containing Hydraulic Cement," Dec. 01, 2023, *ASTM International, West Conshohocken, PA*. doi: 10.1520/C0596-23.
- [28] P. S. Deb, P. Nath, and P. K. Sarker, "Drying Shrinkage of Slag Blended Fly Ash Geopolymer Concrete Cured at Room Temperature," *Procedia Eng*, vol. 125, pp. 594–600, 2015, doi: 10.1016/j.proeng.2015.11.066.
- [29] N. Kozhageldi *et al.*, "Properties of Geopolymer Mortar Mixtures Containing Waste Glass Aggregates and River Sand," *Key Eng Mater*, vol. 945, pp. 93–99, May 2023, doi: 10.4028/p-67b121.
- [30] M. Dineshkumar and C. Umarani, "Effect of Alkali Activator on the Standard Consistency and Setting Times of Fly Ash and GGBS-Based Sustainable Geopolymer Pastes," *Advances in Civil Engineering*, vol. 2020, no. 1, Jan. 2020, doi: 10.1155/2020/2593207.
- [31] "Test Method for Potential Alkali Reactivity of Aggregates (Mortar-Bar Method)," Nov. 15, 2023, *ASTM International, West Conshohocken, PA*. doi: 10.1520/C1260-23.
- [32] M. U. Salim and M. A. Mosaberpanah, "The mechanism of alkali-aggregate reaction in concrete/mortar and its mitigation by using geopolymer materials and mineral admixtures: a comprehensive review," *European Journal of Environmental and Civil Engineering*, vol. 26, no. 14, pp. 6766–6806, Oct. 2022, doi: 10.1080/19648189.2021.1960899.
- [33] H. Taghvayi, K. Behfarnia, and M. Khalili, "The Effect of Alkali Concentration and Sodium Silicate Modulus on the Properties of Alkali-Activated Slag Concrete," *Journal of Advanced Concrete Technology*, vol. 16, no. 7, pp. 293–305, Jul. 2018, doi: 10.3151/jact.16.293.

Information about authors:

Zhuzimkul Urkinbayeva – Senior Lecturer, Department of Technology of Industrial and Civil Engineering, L.N. Gumilyov Eurasian National University, Astana, Kazakhstan, zhuzim.isina@mail.ru

Assel Jexembayeva – PhD, Director, Department of Innovative Development, L.N. Gumilyov Eurasian National University, Astana, Kazakhstan, jexembayevaassel@gmail.com

Marat Konkanov – PhD, Director, Science and Production Centre "ENU-Lab", L.N. Gumilyov Eurasian National University, Astana, Kazakhstan, marcon@metrology.kz

Samal Akimbekova – PhD Student, Department of Technology of Industrial and Civil Engineering, L.N. Gumilyov Eurasian National University, Astana, Kazakhstan, sammi_ok@mail.ru

Lailya Zhaksylykova – MSc, Acting Associate Professor, Department of Architecture, L.N. Gumilyov Eurasian National University, Astana, Kazakhstan, sabyrbayeva_la@enu.kz

Tariq Umar – PhD, Professor, School of Architecture and Environment, University of the West of England, Bristol, United Kingdom, tariqumar1984@gmail.com

Author Contributions:

Zhuzim Urkinbaeva – concept, methodology, testing, drafting.

Assel Jexembayeva – resources, funding acquisition.

Marat Konkanov – resources, funding acquisition.

Samal Akimbekova – data collection, analysis, editing.

Lailya Zhaksylykova – modeling, visualization.

Tariq Umar – concept, interpretation.

Conflict of Interest: The authors declare no conflict of interest.

Use of Artificial Intelligence (AI): The authors declare that AI was not used.

Received: 14.02.2025

Revised: 27.06.2025

Accepted: 27.06.2025

Published: 28.06.2025



Copyright: © 2025 by the authors. Licensee Technobius, LLP, Astana, Republic of Kazakhstan. This article is an open access article distributed under the terms and conditions of the Creative Commons Attribution (CC BY-NC 4.0) license (<https://creativecommons.org/licenses/by-nc/4.0/>).



Corrigendum to “A. Omarov and Y. Iwasaki, “Comparative study of pile quality control techniques”, tbus, vol. 4, no. 1, p. 0055, Mar. 2024. doi: 10.54355/tbus/4.1.2024.0055”

In the originally published version of this article, the following corrections have been made:

In the Abstract, the sentence:

“...with 1,896 bored piles subjected to rapid testing. Significant findings reveal that approximately 75% of tested shafts exhibited anomalies, emphasizing the necessity for meticulous quality control...”

was inadvertently included and has now been removed to accurately reflect the scope and content of the study.

In the paragraph preceding Figure 5, the phrase:

“...and financial support of L.N. Gumilev ENU and KGS LLP...”

has been revised to read:

“...support of KGS-Astana LLP...”

to correct the source of technical support.

In the same paragraph, additionally, the sentence:

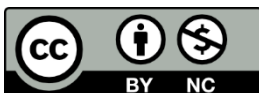
“A total of 1,896 bored piles were tested between February and October 2018...”

was excluded to align with the finalized dataset and timeframe discussed in the article.

These corrections do not affect the overall conclusions of the article.

The authors apologize for any confusion this may have caused.

Published: 28.06.2025



Copyright: @ 2025 by the authors. Licensee Technobius, LLP, Astana, Republic of Kazakhstan. This article is an open access article distributed under the terms and conditions of the Creative Commons Attribution (CC BY-NC 4.0) license (<https://creativecommons.org/licenses/by-nc/4.0/>).